

REVIEW ARTICLE

Open Access

Fluorescence microscopic visualization of functionalized hydrogels

Jinpan Zhong¹, Tianyi Zhao¹ and Mingjie Liu¹

Abstract

Functionalized hydrogels play an important part in chemistry, biology, and material science due to their unique microstructures. Characterization of these microstructures is the fundamental issue to improve the optical, mechanical, and biochemical performance of functionalized hydrogels. With the rapid development of fluorescence microscopy, a growing number of researchers have attempted to utilize this easily operated, noninvasive, and high-contrast technique to visualize the fine microstructure of hydrogels. Integration of a confocal system into fluorescence microscopy allows the sectioning and reconstruction of 3D hydrogel networks. The live recording function offers in situ and real-time images of dynamic behaviors within hydrogels. The development of super-resolution fluorescence microscopy has significantly promoted imaging quality from the submicron scale to the nanoscale. Based on these spectacular achievements, we reviewed the recent advances in fluorescence microscopic visualization of internal morphologies, mechanical properties, and dynamic structural changes. The scope of this review is to provide inspiration for researchers in chemistry, material science, and biology to study and fabricate functionalized hydrogels with the assistance of fluorescence microscopic visualization.

Introduction

Hydrogel-based artificial materials possess the intrinsic characteristics of a high water content and softness are hydroscopic, thixotropic, elastic, and biocompatible¹. These extraordinary properties have boosted the rapid development of functionalized hydrogels in a variety of chemical and biological applications, such as tissue engineering², drug delivery³, 3D printing⁴, and soft robotics⁵. To further optimize the functionality and broaden the application prospects of hydrogels, advanced characterization techniques are urgently required for a deeper understanding of the structure–function relationship. In comparison with spectroscopic and macroscopic methods, microscopic techniques are capable of visualizing the hydrogel microstructure in a direct manner. In earlier research, electron microscopy was utilized to provide

nanoscale 2D micrographs of 3D hydrogel networks, but drying treatment for sample preparation is necessary⁶. This limitation hinders observation of the native morphology of the hydrogel microstructure and dynamic structural changes. Therefore, alternative microscopic techniques must be established to meet the requirements of in situ and real-time visualization in aqueous environments.

In recent decades, fluorescence microscopy has undergone a booming development from widefield fluorescence microscopy to confocal laser scanning microscopy (CLSM) and then to super-resolution microscopy^{7–10}. Compared to widefield fluorescence microscopy, CLSM significantly enhanced the image resolution by optical sectioning of a thick sample to avoid the interference of out-of-focus light⁸. To acquire resolutions limited to the realm of electron microscopy, several super-resolution microscopies based on different technical routes were invented^{9,10}. The Nobel Prize in Chemistry in 2014 was awarded to three scientists for their great contributions to the development of superresolved fluorescence

Correspondence: Tianyi Zhao (zhaoty@buaa.edu.cn) or Mingjie Liu (liumj@buaa.edu.cn)

¹Key Laboratory of Bioinspired Smart Interfacial Science and Technology of Ministry of Education, School of Chemistry, Beihang University, 100191 Beijing, P. R. China

© The Author(s) 2022



Open Access This article is licensed under a Creative Commons Attribution 4.0 International License, which permits use, sharing, adaptation, distribution and reproduction in any medium or format, as long as you give appropriate credit to the original author(s) and the source, provide a link to the Creative Commons license, and indicate if changes were made. The images or other third party material in this article are included in the article's Creative Commons license, unless indicated otherwise in a credit line to the material. If material is not included in the article's Creative Commons license and your intended use is not permitted by statutory regulation or exceeds the permitted use, you will need to obtain permission directly from the copyright holder. To view a copy of this license, visit <http://creativecommons.org/licenses/by/4.0/>.

Table 1 Basic properties of different fluorescence microscopy techniques.

Type of instrument	Imaging resolution	Requirement of markers
Widefield fluorescence microscopy	Restricted by Abbe diffraction limit (~250 nm)	Conventional dyes
Confocal laser scanning microscopy	Breaking the Abbe diffraction limit (~200 nm)	Conventional dyes
Super-resolution fluorescence microscopy	Nanoscale resolution (~20 nm)	Ultrastable, photobleaching-resistant dyes

microscopy (Table 1)^{11,12}. These revolutionary achievements inspired material scientists to take advantage of fluorescence microscopic techniques to visualize functionalized hydrogels. The preparation-free nature and easy operation of fluorescence microscopy allow ultrafast, noninvasive, and high-contrast visualization of hydrogel microstructures.

The prerequisite for fluorescence microscopic imaging of hydrogel microstructures is appropriate labeling of the network or aqueous phase. To date, diverse types of fluorophores including organic dyes¹³, fluorescent proteins¹⁴, and nanocrystals¹⁵ have been designed and synthesized. Due to the extensive options, functionalized hydrogels can be rationally modified with fluorophores by covalent bonding, hydrophobic interactions, hydrogen bonding, and electrostatic attraction. The high contrast between labeled and unlabeled phases is probed by fluorescence microscopy for high-quality imaging. Benefiting from the optical sectioning and reconstruction functions of confocal systems⁸, the 3D microstructure of hydrogel networks can be precisely visualized. Dynamic image generation and live video streams provide visualization of the in situ structural changes and real-time matter transport. To investigate hydrogel microstructures with powerful fluorescence microscopy imaging systems, a great number of innovative and impressive imaging strategies have been established to improve the performance of functionalized hydrogels.

In this review, we will summarize the current progress in the structures, properties, and applications of functionalized hydrogels visualized by fluorescence microscopy (Fig. 1). The corresponding topics focus on the internal microstructure and dynamic changes of hydrogel networks, chemical and physical characteristics of hydrogels, and broad applications of functionalized hydrogels. We will provide our thinking and predictions on future challenges and the development of fluorescence microscopic strategies for visualizing functionalized hydrogels. The goal of this review is to provide viable opportunities and inspirations for researchers from a wide range of disciplines.

Internal microstructure of hydrogels

Comprehensive investigation of the internal microstructures of hydrogel networks is of particular interest

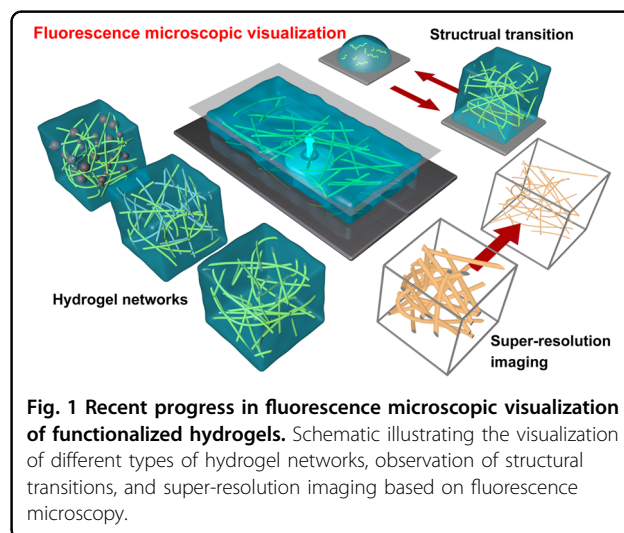
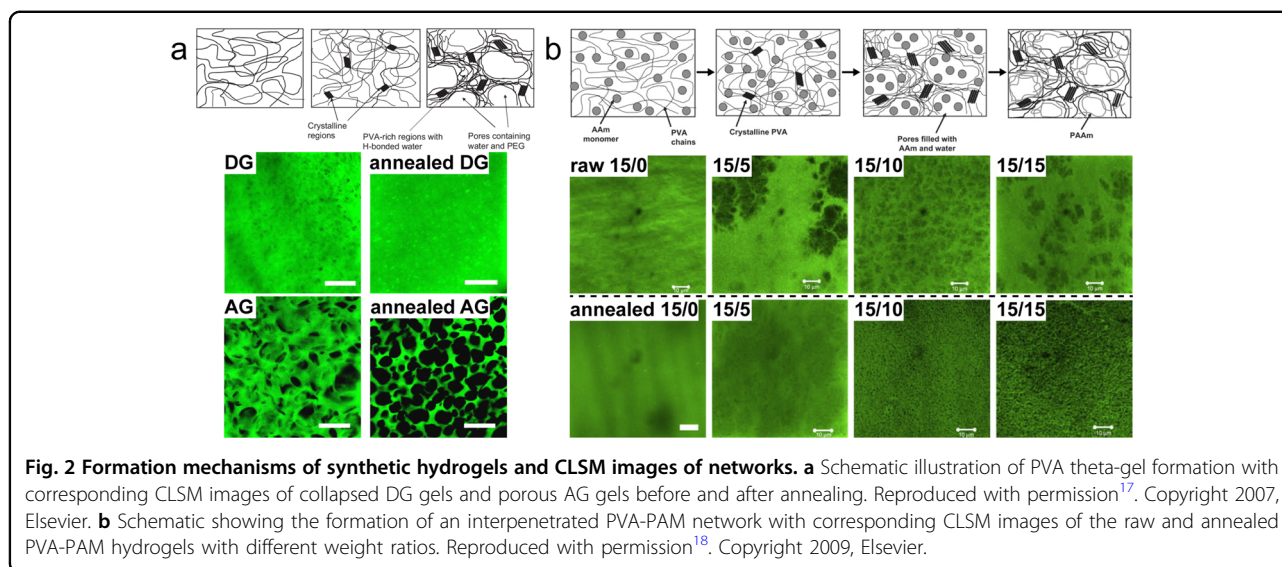


Fig. 1 Recent progress in fluorescence microscopic visualization of functionalized hydrogels. Schematic illustrating the visualization of different types of hydrogel networks, observation of structural transitions, and super-resolution imaging based on fluorescence microscopy.

for the regulation of chemical, physical, and biological performance. Characterization methods based on visualization techniques are the most direct route to study these hydrogel microstructures. Among the visualization techniques, fluorescence microscopy has raised great attention in recent decades due to its characteristics, such as high contrast, noninvasiveness, no required preparation, and simple operation. Thus, a growing number of studies have reported the design and application of novel fluorescence visualization strategies for understanding and improving the properties of functionalized hydrogels. Since hydrogels usually lack fluorescence emission ability, fluorescent markers should be attached to the chains before or after the synthesis of hydrogels. For example, 5-(4,6-dichlorotriazinyl) aminofluorescein (DTAF) is widely used as a fluorescent indicator by forming covalent bonds with the primary hydroxyl groups of a variety of hydrogels. Accordingly, the internal microstructures of hydrogels stained with appropriate fluorophores can be successfully visualized by fluorescence microscopy.

Synthetic hydrogel networks

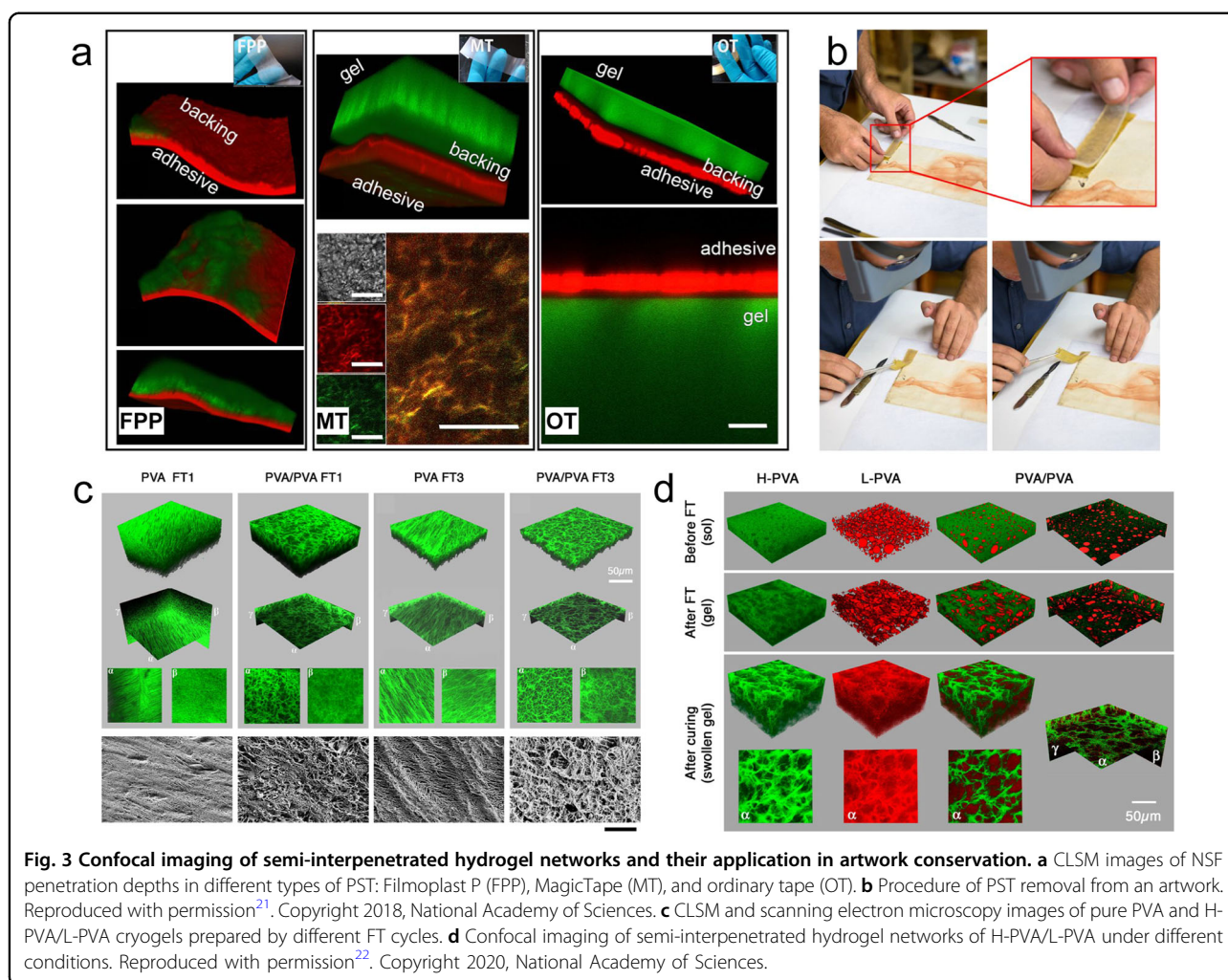
Microscopic investigation of the continuous, bulk, and 3D networks of poly(vinyl alcohol) (PVA) originating from freezing-induced phase separation was accomplished by confocal imaging. Covalently labeled PVA



networks with DTAF showed the formation of water-rich and PVA-rich phases, implying that phase separation resulted from spontaneous spinodal decomposition after cooling. Confocal images captured at different depths demonstrated that the network is composed of a thin surface with a thickness of a few microns and a bulk phase with uniform porosity. No porosity gradient or structural orientation was observed throughout the entire PVA network. Increasing the PVA concentration led to a smaller pore size and higher tortuosity of the network, which obstructed molecular diffusion¹⁶. Confocal imaging was also applied to study the effect of polyethylene glycol (PEG) on the internal pore morphology of PVA hydrogels by annealing treatment. Physically crosslinked PVA hydrogels were prepared by the theta-gel method, which introduced gelling agents such as low-molecular-weight PEG to force separation and crystallization of PVA without a freeze–thaw (FT) cycle. The as-prepared PVA hydrogel containing PEG was named AG (as-gelled), while the other hydrogel exchanged with water after gelation was named DP (dePEGed). CLSM images indicated that the porous structures of AG gels and the collapsed structures of DP resulted from preservation by PEG during vacuum dehydration and subsequent annealing (Fig. 2a). The crystallinity of both AG and DP gels increased after the annealing step, but the former had a high equilibrium water content (EWC), and the latter showed high creep resistance¹⁷. The application of PVA-based hydrogels for synthetic articular cartilage requires a balance between a high EWC for lubricity enhancement and high creep resistance for mechanical stability. A hydrophilic polymer, polyacrylamide (PAM), was added to replace PEG to increase the lubricity and strength of the interpenetrated network by increasing water uptake and filling the pores. Fluorescence imaging showed that the

pores of PVA-PAM gels were more uniform and smaller than those of PVA-PEG gels and that the pore size increased with increasing PAM content (Fig. 2b). Based on this guidance, PVA-PAM gels with higher creep resistance and lower relative coefficient of friction were obtained at lower PAM contents because of the less reduced crystallinity of PVA and higher permeability upon loading¹⁸.

The spatial resolution of CLSM is close to submicron; therefore, super-resolution fluorescence techniques overcoming the diffraction limit of light come into use. Stochastic optical reconstruction microscopy (STORM) is capable of sub-diffraction-limit imaging based on high-accuracy localization of photoswitchable fluorophores¹⁹. Overall, STORM images with a super-resolution of 20 nm were obtained by reconstructing the locations of the entire population of fluorophores. Due to the molecular-scale resolution of this technique, STORM has become a versatile tool for biological imaging applications. Recently, this technique has been applied to the visualization of hydrogel networks due to the flexibility of labeling and capability of working in aqueous environments. Interpenetrated hydrogel networks were synthesized by coextrusion of functionalized precursors based on thermoresponsive poly(*N*-isopropylacrylamide) (PNIPAM) and nonthermoresponsive poly(vinyl pyrrolidone) (PVP). Detailed thermoresponsive phase segregation morphology visualized by direct stochastic optical reconstruction microscopy (dSTORM) indicated that PNIPAM-rich domains were entrapped in the clustered PVP-rich phase, which was consistent with the small-angle neutron scattering (SANS) results. The combination of dSTORM and SANS provided a deeper understanding of the internal morphology of interpenetrated hydrogel networks across multiple resolution scales to



guide the fabrication of more effective interpenetrated structures²⁰.

Semi-interpenetrated hydrogel networks are regarded as a safe cleaning tool for the conservation of artworks due to the residue-free and noninvasive nature of these materials. Structural visualization of semi-interpenetrated networks is fundamental to the analysis of matter exchange during cleaning processes. Illumination of these networks can be accomplished by specific fluorescence labeling of solvents (rhodamine 110 or Nile-red) or hydrogel matrices (covalently modified by rhodamine B isothiocyanate or fluorescein isothiocyanate). Recent work has reported a colloidal cleaning system featuring confinement of nanostructured fluids (NSFs) in hydrogel networks for removing pressure-sensitive tape (PST) from paper artworks²¹. 3D fluorescence imaging of labeled hydrogels and PSTs demonstrated that the penetration depths of NSFs depended on the hydrophilic and hydrophobic compositions of the PST (Fig. 3a). This

observation contributed to the control of solvent penetration and lateral migration of the liquid phase, which guaranteed a versatile removal process of PST (Fig. 3b). Another semi-interpenetrated hydrogel network composed of high-molecular-weight PVA (H-PVA) and low-molecular-weight PVA (L-PVA) was designed to remove dirt from modern and contemporary art²². 3D reconstruction fluorescence images showed that FT treatment led to a homogeneous arrangement of pseudo-hexagonally packed smaller pores for pure H-PVA and a nonordered sponge-like network for semi-interpenetrated H-PVA/L-PVA (Fig. 3c). In the semi-interpenetrated networks, decoiled and solvated H-PVA constituted the gel wall through intermolecular hydrogen bonding, while L-PVA chains collapsed into spherical droplets (Fig. 3d). This twin-chain hydrogel microstructure with ideal mechanical properties, retentiveness, and interconnected porosity guaranteed adhesion to paint layers, control of surface wetting, and safe removal of dirt.

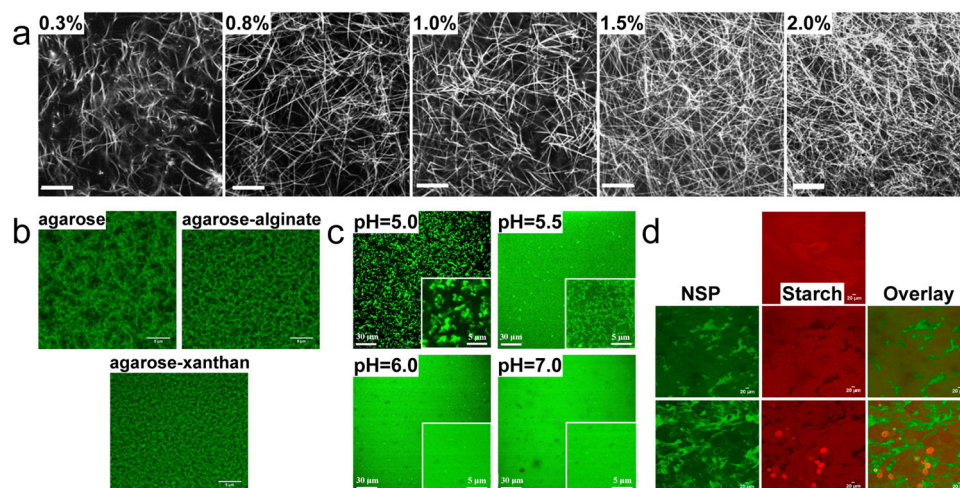


Fig. 4 Confocal imaging of biomacromolecular hydrogel networks. **a** CLSM images of collagen fibers at different concentrations. Reproduced with permission²⁵. Copyright 2010, Elsevier. **b** CLSM images of agarose gels with different thickeners: agarose, agarose-alginate, and agarose-xanthan. Reproduced with permission²⁶. Copyright 2013, American Chemical Society. **c** CLSM images of mixed XG/GB hydrogel networks at different pH values. Reproduced with permission²⁸. Copyright 2016, Elsevier. **d** CLSM images of potato starch and nonstarch polysaccharide (NSP) composite gels: potato starch, agar-potato starch, and konjac glucomannan-potato starch (from top to bottom). Reproduced with permission²⁹. Copyright 2021, Elsevier.

Biomacromolecular hydrogel networks

The internal microstructures of several biomacromolecular hydrogels have been visualized by fluorescence imaging to design biocompatible materials. For example, earlier research studied the influencing factors of neuronal outgrowth in isotropically and magnetically aligned fibrin gels by confocal imaging. Visualization of the fluorescently spiked fibrin network showed that a higher concentration of Ca^{2+} led to a larger fibril diameter without changing the alignment degree. The combination of CLSM with other characterization techniques provided important information for designing entubulation repair materials based on magnetically aligned fibrin gels²³. Recently, a novel method based on the combination of CLSM with a fiber extraction algorithm and turbidity measurements was proposed to study the relation between the structure and diffusivity of solutes within the fibrin network. The fiber extraction algorithm quantitatively analyzed the fluorescence images of fibrin networks to determine the average fiber length, total fiber length, hydrogel fiber density, branch density, and fiber connectivity. This quantitative structural analysis demonstrated that changes in the concentrations of fibrinogen, thrombin, factor XIII, and calcium resulted in significant variations in the overall network organization and individual fiber characteristics but only a moderate influence on the relative diffusivity of dextran solutes. Based on these findings, the structural, diffusional, and mechanical characteristics of fibrin hydrogels could be tailored by changing the concentrations of individual constituents for specific applications in tissue engineering²⁴. The

structural and mechanical properties of a 3D scaffold comprised of dense type I collagen and endothelial cell biology within the scaffold were studied by fluorescence imaging. Confocal images of the collagen network showed that an increased concentration of collagen could increase only the spatial density of fibers rather than the fiber diameter, indicating that the larger modulus resulted from more fiber entanglement (Fig. 4a). Thus, the window of collagen concentrations was determined for microfabrication and cellular remodeling to control the spatiotemporal chemistry and hydraulic stresses of the scaffold. Integrating microfluidic control within such scaffolds showed the potential for studying spatiotemporal signaling during tumor angiogenesis and vascularized tissue engineering²⁵.

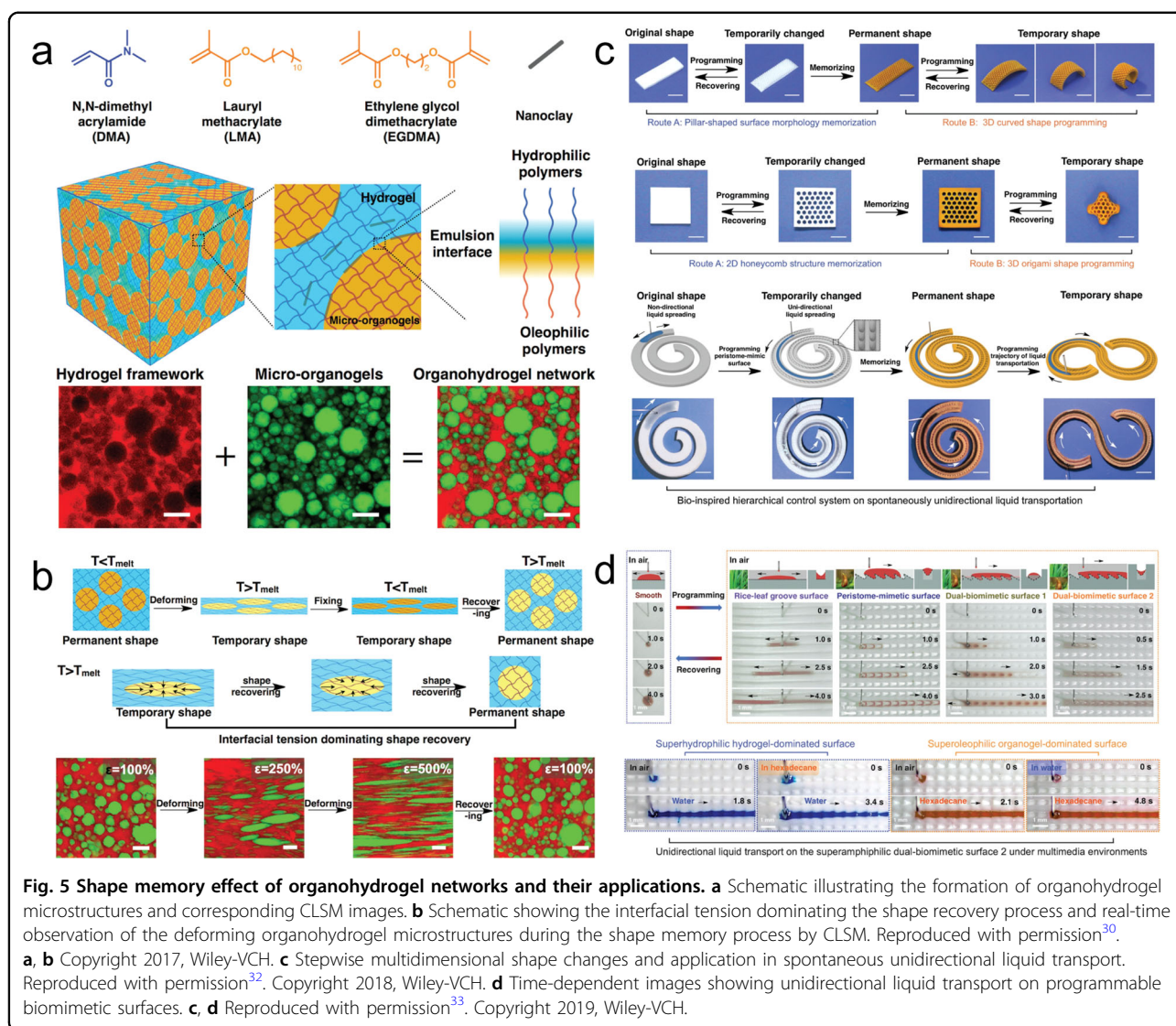
Polysaccharide hydrogels are widely used as stabilizers, thickeners, and the main structure-forming ingredients in the food and pharmaceutical industries for quality improvement and cost reduction. In most practical applications, mixtures of polysaccharide hydrogels are used to manipulate the material properties by interactions and entanglement of individual components. Microscopic visualization of the internal network of polysaccharide hydrogels provided important insight into the structure-effective relationship to optimize the quality of food and pharmaceutical products. Compared to indirect methods, such as textural and rheological measurements, fluorescence microscopic imaging could visualize the distribution and interaction of individual components in multicomponent food matrices. Several studies have reported the fluorescence visualization of

polysaccharide mixtures based on DTAF staining methods. Incorporation of nongelling thickeners into the networks of gelling agents is known to alter the viscoelasticity, gelling temperature, and thermal stability of the resulting hydrogel composites for a wider range of mechanical properties. For example, incorporation of alginate and xanthan into an agarose hydrogel network had a significant impact on the gelation mechanism and thermomechanical properties. Confocal imaging of the agarose hydrogels selectively labeled with DTAF indicated that the addition of the thickeners increased the homogeneity of the network (Fig. 4b). Combining the results of fluorescence imaging and rheology measurements, it was discovered that the weak network of the agarose gel with homogeneously and equally distributed meshes was stabilized by interpenetrated alginate coils. In contrast, rod-like xanthan formed stiff and rigid obstacles to disturb the coil and helix diffusion of agarose chains during gelation, resulting in a less elastic network²⁶. As it is difficult to distinguish the different phases of systems containing multiple hydrogel components with similar properties, a staining method with DTAF was developed to visualize the microstructures in mixed systems. Fluorescence imaging showed that DTAF selectively stained low acyl gellan and simultaneously ensured that the secondary PVA hydrogel remained unstained. The addition of DTAF to the gellan backbone increased the mechanical properties and resulted in phase separation of the mixture. Thus, this method should be employed as a validation method of the investigated structure to supplement other analytical techniques²⁷. Despite the limitations in polysaccharide-polymer systems, the DTAF staining method was successfully applied to polysaccharide-protein and polysaccharide-polysaccharide systems. To design novel thickeners and gelling agents, synergistic gelation of a polysaccharide-protein system consisting of xanthan gum (XG) and gelatin B (GB) was reported. Rheological and microstructural research was conducted to achieve a balance between electrostatic attraction and repulsion to maximize the mechanical properties. Confocal images of XG covalently labeled with DTAF and GB stained with Nile Blue A showed that the mixed XG/GB hydrogel network at pH 5.5 had the smallest characteristic microstructural length scale to obtain the most favorable gelling properties (Fig. 4c). Gelation at lower or higher pH values resulted in strong electrostatic attraction-induced aggregation or electrostatic repulsion-induced phase separation. Furthermore, the addition of salt into the XG/GB network at pH 5.5 could break down the network structure into particles, explaining the sudden decrease in rheological properties. CLSM images, zeta potentials, visual inspection, and the rheological results collectively demonstrated that the microstructure and corresponding

rheological properties of this polysaccharide-protein system were driven by electrostatic forces that could be controlled by pH and ionic strength²⁸. The microstructure of polysaccharide-polysaccharide hydrogels and the distribution of individual components were visualized by confocal imaging of DTAF-labeled polysaccharides with different anionic groups. Multiple characterization techniques verified that the labeling of polysaccharides with DTAF had the following advantages: availability in aqueous environments, no impact on the sol-gel transition temperature or gel strength of polysaccharides, and long-term stability as a powder at room temperature. Fluorescence imaging of the mixed network demonstrated that DTAF labeled polysaccharides and confirmed that the secondary polysaccharides remained unstained (Fig. 4d). Therefore, the component distribution, compatibility of mixed polysaccharides, and network formation were directly visualized by CLSM in both hydrated and dehydrated forms²⁹.

Organohydrogel networks

Organohydrogels are a new class of functional materials composed of micro-organogels uniformly dispersed in hydrogel networks. A synergistic fabrication strategy imitating natural biological systems has inspired researchers to synthesize functionalized organohydrogels based on biphasic heterostructures. Diverse characterization techniques were utilized to study heterostructures composed of hydrophobic micro-organogels and a hydrophilic hydrogel matrix. In particular, fluorescence imaging provided high-contrast structural information by visualizing the two domains with specific fluorophores. Several recent works reported the microscopic visualization of binary cooperative phases in organohydrogels and their deformation under strain loading^{30–33}. Highly stretchable shape memory organohydrogels were synthesized by in situ polymerization of oil and aqueous phase emulsion systems. Excellent thermomechanical performance and shape memory effects originated from the synergistic phase transition of micro-organogels and the elastic hydrogel framework. The reinforced mechanical toughness of organohydrogel networks with increasing volume ratio of micro-organogels suggested a possible microsphere morphology of these microdomains. This assumption was directly confirmed by visualizing the preferentially labeled aqueous phase and semicrystalline species (paraffin³⁰ or poly(stearyl methacrylate)³¹) encapsulated in the micro-organogels (Fig. 5a, b). Shape memory behaviors were based on the thermoresponsive phase transition of paraffin or poly(stearyl methacrylate) encapsulated in the micro-organogel domains. The shape memory and recovery process were divided into three steps: (i) elongation at temperatures above the melting point (T_m) by softening the organohydrogel domains; (ii)

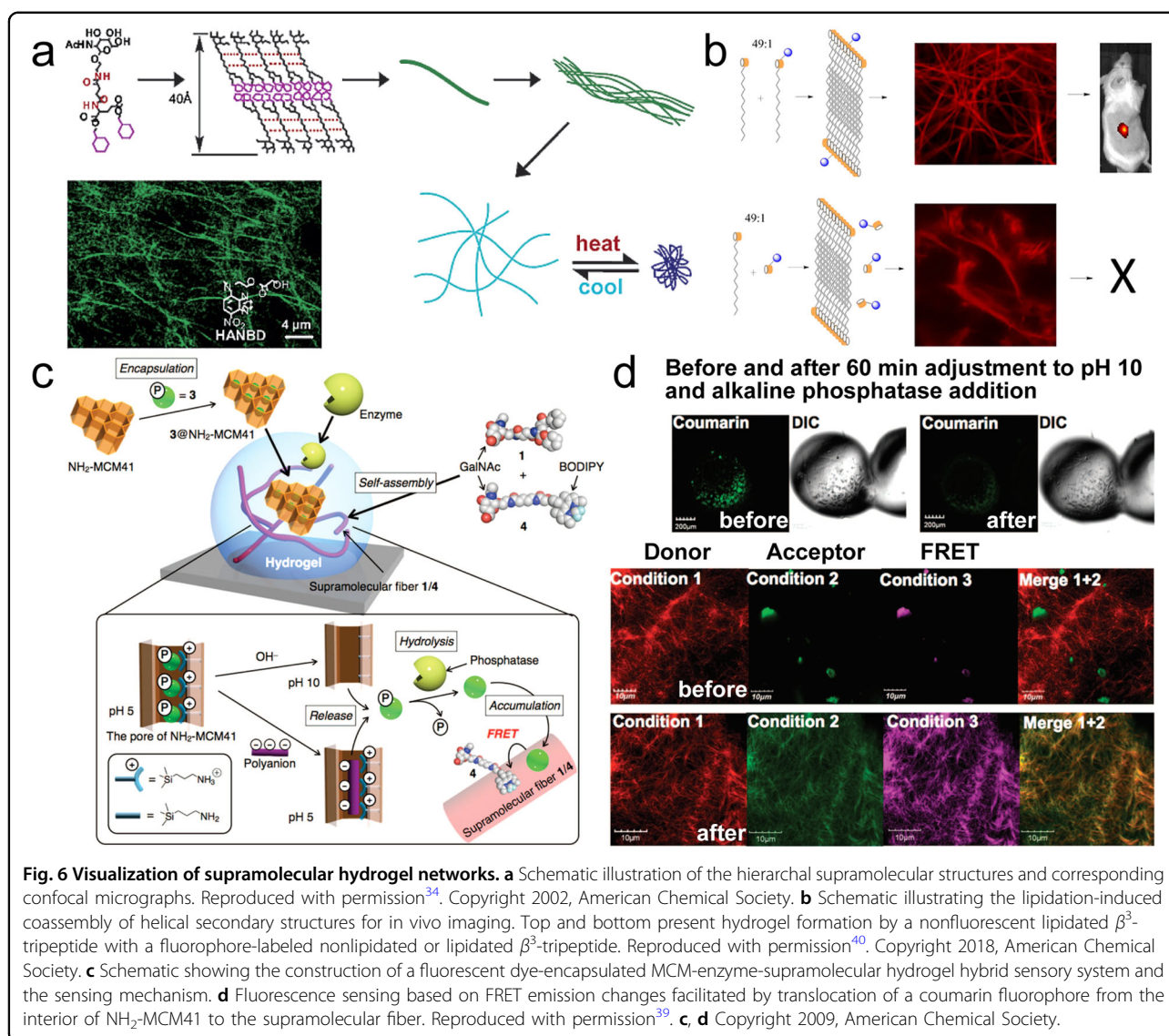


fixation of the temporary shape by cooling below T_m ; and (iii) heating above T_m to recover the permanent shape. Corresponding microstructural changes during the whole process were visualized by confocal imaging. Originally, spherical micro-organogels deformed to ellipsoidal shapes upon strain loading, and stripe-like shapes were finally obtained at high elongation. The orientation of the anisotropic heteronetwork was parallel to the direction of stretching, which matched well with the small-angle X-ray scattering measurements. Thus, the organohydrogel was considered to be a spring that stored or released energy when its shape was deformed or recovered. Such thermo-responsive shape memory effects of these organohydrogels were utilized to fabricate smart actuators³² and surface micropatterning³³, showing potential applications in soft robots, flexible electronics, and biomedical devices (Fig. 5c, d).

Supramolecular hydrogel networks

Noncovalent supramolecular hydrogels have the potential to become novel intelligent materials because of their sensitive responses to various physicochemical stimuli. The tunability and recyclability of supramolecular hydrogels are ascribed to the reversible assembly and disassembly of gelators. Screening the structural changes by fluorescence imaging during the phase transition could deepen the understanding of supramolecular chemistry.

Earlier research used CLSM to visualize supramolecular hydrogel networks by specific staining of hydrophobic domains. These amphiphilic supramolecular hydrogel scaffolds were constituted by a small library of low-molecular-weight hydrogelators with glycosylated amino acid derivatives (Fig. 6a). Precise diameters of fiber bundles were measured to determine the robust hydrogen-bonding networks formed by hydrophobic packing. One



of these hydrogels was applied to release water-soluble molecules such as DNA in a thermoresponsive manner or remove hydrophobic water pollutants by coprecipitation³⁴. Using the same hydrogelator, a novel semiwet peptide/protein microarray was fabricated by spontaneous gel formation. Aqueous cavities in the gel matrix and hydrophobic domains of the fibers were confirmed by CLSM imaging of an environmentally sensitive fluorescent probe entrapped in the amphiphilic network. This semiwet structure could entrap enzymes in the hydrophilic microcavities without substantial loss of activity and bind hydrophobic molecules within the fibers. Based on the enzymatic hydrolysis-induced fluorometric activity, peptide/protein-hydrogel arrays compatible with enzyme activity assays were built to screen enzyme inhibitors. Compared to conventional protein/peptide chips, supramolecular hydrogel arrays are free from chemical

attachment of protein/peptide to a two-dimensional and dried substrate, improving the sensitivity and signal/noise ratio³⁵. This powerful strategy was rationally extended to the design of several read-out modes (fluorogenic probe, environmentally sensitive probe, and Förster resonance energy transfer (FRET)-type pair) for evaluating enzymatic activity³⁶. The combination of two similar hydrogelators from the library contributed to the formation of a pH-responsive supramolecular hydrogel in which one hydrogelator provided a stable hydrogel structure and the other acted as a pH stimulus-sensitive trigger. The fibrous microstructure of the mixed hydrogel network was visualized by staining hydrophobic domains with an environmentally sensitive dye. Fluorescence spectra analysis of the selected region in CLSM images enabled interpretation of the hydrophobicity around the position of the dye by different emission peaks. This

supramolecular hydrogel was further applied to the controlled release of water-soluble bioactive substances by pH-triggered expulsion of water³⁷. The cooperation of semiwet supramolecular hydrogels with artificial receptors produced an efficient molecular recognition system for sensing and discriminating phosphate derivatives. Colocalization and time-dependent analysis by confocal imaging directly demonstrated that the location of receptors could dynamically switch between hydrophobic hydrogel fibers and hydrophilic aqueous cavities upon guest binding. On this basis, three distinct types of discrimination systems were proposed for sensing phosphate derivatives: (i) a photoinduced electron transfer type, (ii) an environmentally sensitive type, and (iii) an artificial FRET type. Extension of these systems for rapid and high-throughput sensing of phosphate derivatives was accomplished by analyzing fluorescence intensity changes, fluorescence wavelength shifts, and ratiometric fluorescence changes³⁸. Another novel hybrid sensing system for discriminating polyanions was developed based on the combination of a semiwet supramolecular hydrogel matrix, enzymes, and mesoporous silica particles (NH₂-MCM41) with anion-exchange ability. Fluorescence imaging showed that the hybrid system was composed of three orthogonally distinct microdomains: cationic nanopores of NH₂-MCM41, hydrophobic nano/microfibers, and the aqueous phase of the hydrogel. Fluorophores entrapped in NH₂-MCM41 were first released by the anion-exchange reaction of polyanions and then translocated to hydrophobic fibers by enzymatic hydrolysis, facilitating the FRET sensing of polyanions (Fig. 6c). Real-time fluorescence imaging directly visualized this sensing mechanism by monitoring dynamic location changes of fluorophores during the sensing process, and colocalization analysis showed fluorophores ultimately located in the hydrophobic core of fibers (Fig. 6d). In summary, the sensitive, cooperative, and high-throughput discrimination ability of the hybrid system was ascribed to the efficient dephosphorylation catalyzed by enzymes, orthogonal formation of distinct domains, and sufficient mobility of the embedded molecules³⁹.

Fluorescence microscopic visualization was also applied to study the supramolecular self-assembly of biomolecules such as peptides and phospholipids. Self-assembling β^3 -tripeptide hydrogels based on noncovalent interactions can be endowed with powerful functionalities by coassembly of monomers with diverse chemical modifications. Confocal and stimulated emission depletion (STED) imaging of the hydrogel networks confirmed the successful coassembly of nonfluorescent lipidated monomers and dye-labeled lipidated monomers by the formation of unique 14-helical secondary structures through hydrogen-bonding interactions (Fig. 6b). β^3 -tripeptide hydrogels covalently modified with a far-red-emitting

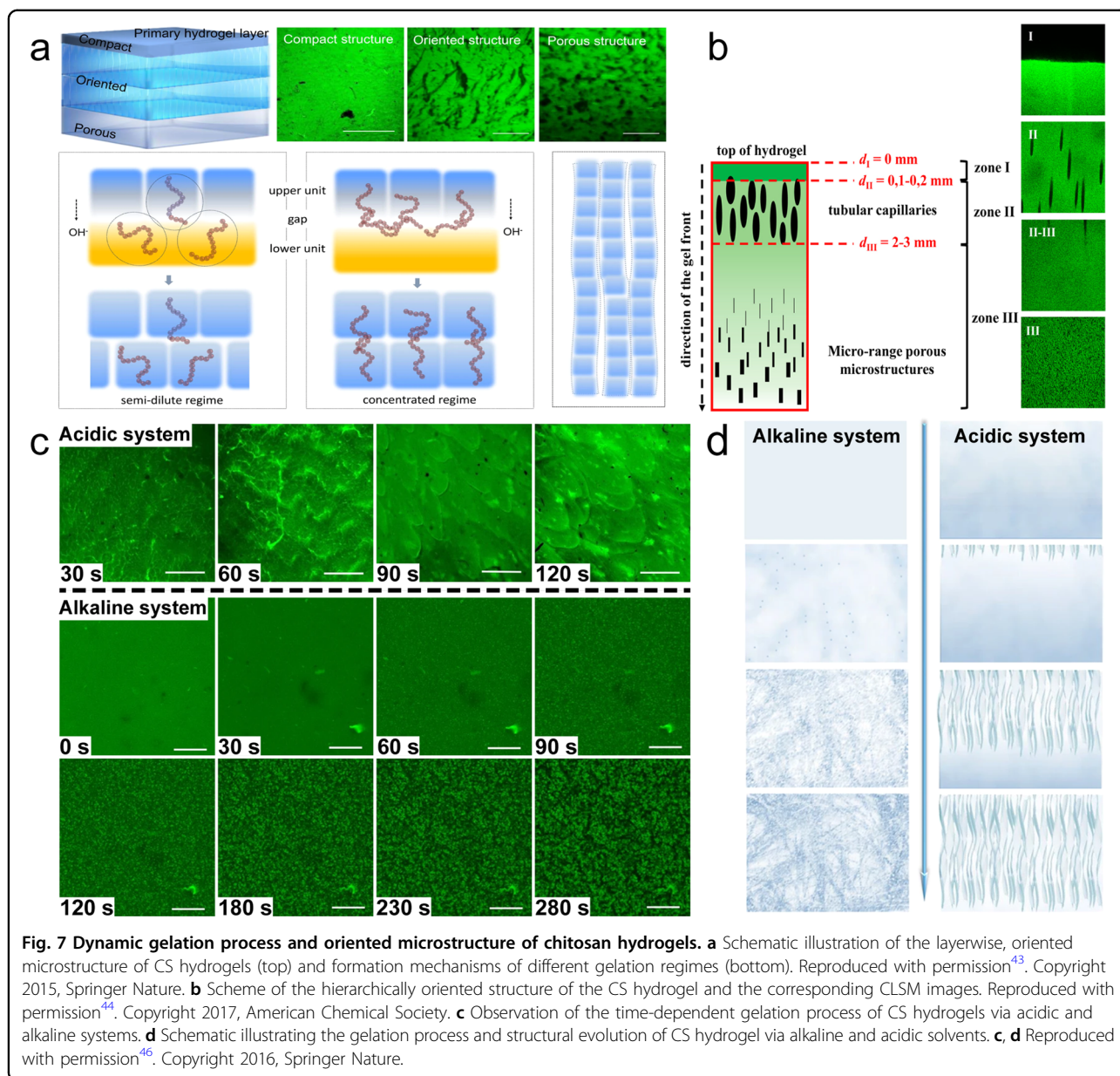
fluorophore were administered to mice via subcutaneous injection for real-time, long-term, and in vivo animal imaging. CLSM imaging of the sectioned gel injection site indicated the integrity of implanted β^3 -tripeptide hydrogels over a 14-day period. The most relevant application of β^3 -tripeptide hydrogels is in vivo fluorescent monitoring for chronic disease involving long-term therapeutic treatment⁴⁰. Another work reported the formation of a helical structure during the dynamic self-assembly process of peptide fibrils studied by STORM. Bulk morphologies of peptide hydrogel networks were visualized within an increased field of view for quantification of the contour and persistence lengths of individual fibrils. By imaging the 2D projection of a 3D structure, STORM removed surface adsorption-induced ambiguity and measured the true structure of fibril networks. Long-term imaging of the two separate fibrils showed no evident monomer exchange over a 4-week period. These results demonstrated the potential applications of STORM in the design of synthetic peptides and the study of self-assembly behaviors⁴¹. A novel hydrogel with a high water content (95%) was formed by supramolecular aggregation of phospholipids and fatty acids. By controlling the pH of the lipid dispersion, phospholipid mixtures tended to form supramolecular hydrogels with a microscopically spongy morphology rather than vesicular or micellar aggregates. Confocal imaging and cryogenic transmission electron microscopy showed that the hydrogel network was composed of aggregates of giant multilamellar vesicles (5–20 μm diameter) with the coexistence of nanosized unilamellar vesicles (150 nm diameter). This structured but easily deformable hydrogel has promising prospects in topical and ocular applications requiring the incorporation of either lipophilic or hydrophilic drugs⁴².

Structural changes of hydrogels

The chemical and physical properties of functionalized hydrogels can be easily altered by structural changes, such as gelation processes, sol-gel/gel-sol transitions, and phase separation. Direct visualization of these dynamic structural changes will deepen the understanding of the structure–function relationship. The in situ and real-time characteristics of fluorescence microscopy offer an ideal platform to visualize these structural changes at the microscale. Benefiting from the dynamic screening function of fluorescence microscopy, an increasing number of visualization strategies have been successfully established to study the mechanisms of the gelation process, regulation of self-assembly behaviors, and control of matter release.

Gelation process of synthesized hydrogels

The gelation process of chitosan (CS) hydrogels by alkaline neutralization of solubilized CS in acidic aqueous



medium was visualized by fluorescence microscopic imaging^{43,44}. This synthesis route contributed to the formation of a hierarchically oriented structure along the diffusion direction of OH⁻. Confocal imaging of the labeled CS hydrogels showed that the oriented microstructure evolving from the surface to the bulk could be divided into three gelation regimes that were separated by two structural transition zones (Fig. 7a). The first zone close to the surface was a smooth and compact layer constituted by entangled CS chains due to fast neutralization. The second zone was composed of some large pores or capillaries oriented parallel to the advancing direction of OH⁻. In the third zone, a finer oriented microstructure with uniform porosity replaced the

capillary morphology because of the decreased advancing rate of OH⁻ (Fig. 7b). Thus, the layerwise characteristics of the microstructure could be considered as the stacking of numerous hydrogel layer units along the OH⁻ diffusion direction. The corresponding formation mechanism was proposed based on the dynamic macromolecular interaction in CS-rich microzones, water-rich microzones, and equilibrium phase where homogeneous CS solution contacted OH⁻. It was concluded that the formation of an oriented microstructure required sufficient entanglement of macromolecular chains and a proper diffusion rate of OH⁻. CS hydrogels synthesized by this method facilitated the fabrication of hydrogel materials with enhanced mechanical performance and modulated molecular

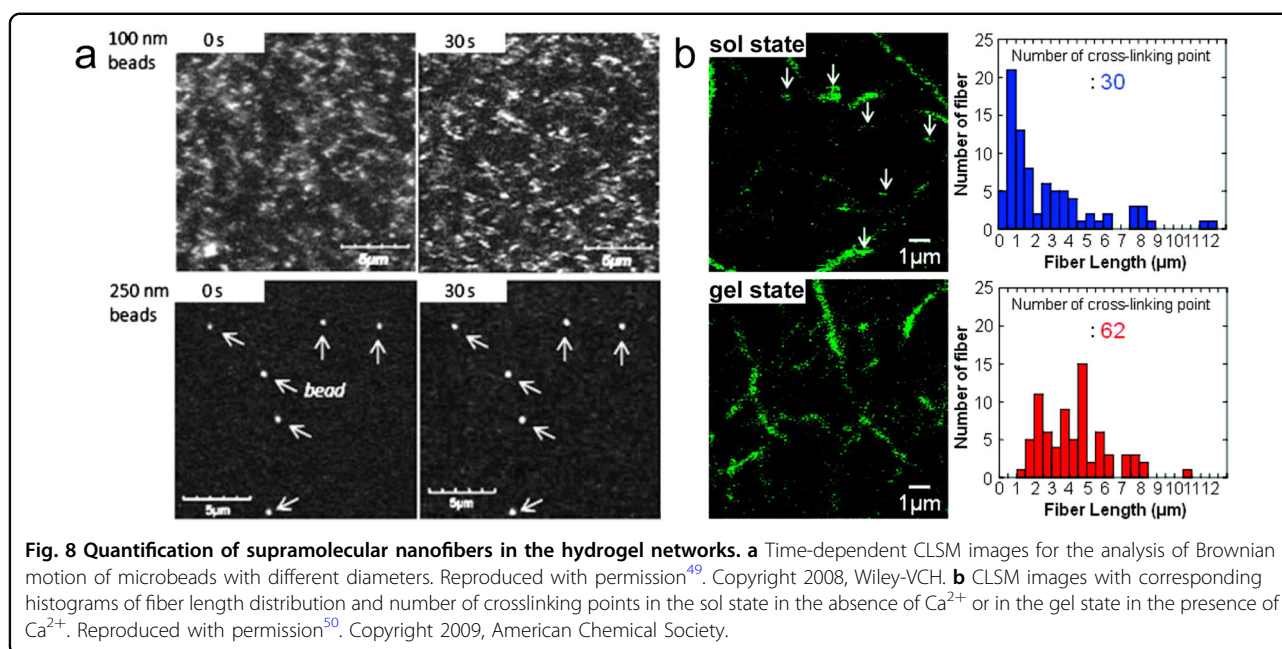
transport for potential applications in cellular colonization and migration.

The gelation process of chitosan in LiOH-urea solution was entirely visualized by fluorescence imaging of tetraphenylethene moieties attached to the hydrogel chains. In situ visualization of the fluorescent patterns of hydrogel networks by CLSM demonstrated that the gelation process could be divided into two stages: a thermal gelation stage and a rinse stage. Accompanied by other pseudo-in situ investigations, it was confirmed that the dynamic variations in hydrogen bonding between hydroxide ions, urea, and chitosan dominated the development of junction points and the formation of crystals. This work highlighted the possibility of visualizing different gelation systems by fluorescence imaging to better understand the gelation process⁴⁵. In situ confocal imaging was further applied to investigate the different gelation processes of CS hydrogels via acidic and alkaline solvent systems. Real-time confocal imaging showed that the roughness in acidic systems increased with increasing gelation time, demonstrating that the gelation mechanism was deprotonation and entanglement of CS macromolecules into fibrous structures. In comparison, the alkaline system evolved integrally by intermolecular hydrogen bonding during a gelation process composed of a thermal gelation stage and a rinse stage (Fig. 7c). The significant difference between gelation mechanisms of acidic and alkaline systems led to CS hydrogels with different hierarchical structures. CLSM micrographs indicated that the acidic system had an oriented fibrous hydrogel structure with compact voids, while the alkaline system had a homogeneous network structure at the nanoscale (Fig. 7d). Such homogeneous, oriented, and fibrous 3D hydrogel networks of alkaline systems possessed a uniform distribution of strain loading and reduced structural defects, showing great improvements in hardness, strength, and toughness⁴⁶. Fluorescence imaging was also used to study the gelation process of inorganic hydrogel composites by employing the bicontinuous self-assembly of mixed laponite and montmorillonite dispersions. In situ imaging of gelation kinetics by CLSM showed the evolution of a 3D microporous architecture with increased gelation time and ultimately an interconnected network. The fluorescence location of two platelets labeled with different dyes combined with TEM and rheology results synergistically verified that the microstructure of the hydrogel network consisted of overlapping coins or house-of-card configurations (larger montmorillonite platelets form the network surrounded by small laponite platelets). Additionally, a higher mixing ratio of laponite to montmorillonite increased the pore size and therefore enhanced the strength of the composite network. CLSM micrographs showed that the rupture of the network at the transition temperature was ascribed to the collapse at

the microscale induced by weakened interaction within local gel domains. Such unique and tunable properties were envisioned for specific applications, such as lithium battery design, nuclear waste management, and flame-retardant materials⁴⁷. With the instrumental development of confocal systems, a multimodal approach based on the integration of CLSM, confocal reflectance microscopy (CRM), and confocal rheology was established to investigate the fibrillogenesis of type I collagen during the sol-gel transition. Simultaneous fluorescence imaging and rheological measurements over the course of fibrillogenesis allowed synergistic analysis of the structural evolution and viscoelastic variations. A comparison of microscopic and rheological data as well as further quantitative analysis verified the presence of a so-called system-spanning structure, which was inconsistent with the predictions of percolation theory. Despite such notable discrepancies, the utility of multimodal measurements for quantitative analysis of evolving structural and viscoelastic properties of hydrogel networks could serve as critical test beds to control properties of self-assembling systems⁴⁸.

Phase transition of supramolecular hydrogels

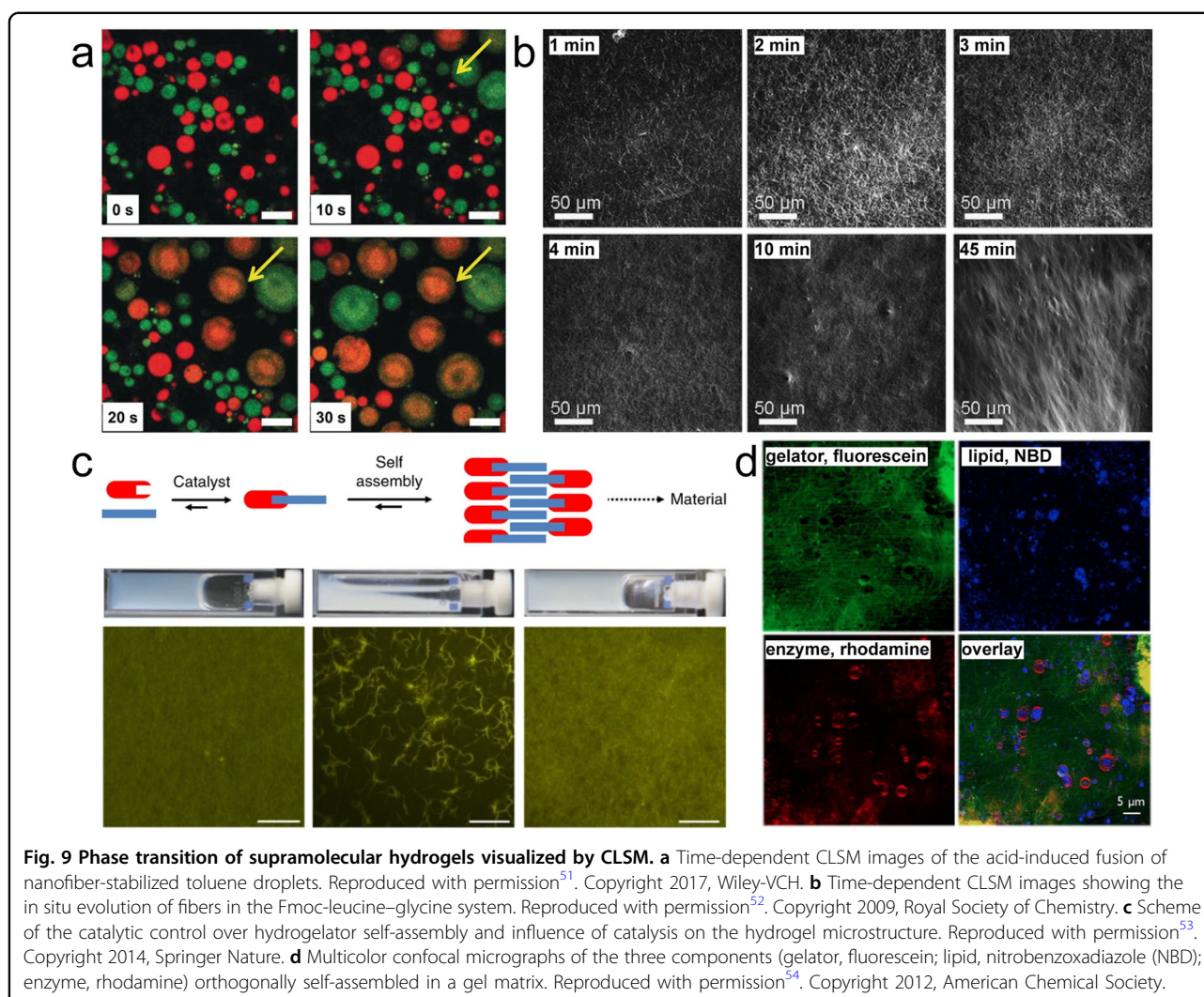
Fluorescence microscopic imaging has also been applied to study the important sol-gel/gel-sol transitions of synthesized supramolecular hydrogels. Direct 3D visualization of hydrogel networks by CLSM showed a significant structural difference between the sol state and gel state. Interestingly, an indirect measurement method was proposed to estimate the mesh size of hydrogel networks by observing the Brownian motion of fluorescent nanobeads with different diameters in the matrix (Fig. 8a). This method was further applied to study the bacterial and enzymatic movement controlled by photoresponsive supramolecular nanomeshes⁴⁹. From the above results, a fine-tuned release strategy was established based on the multiple response (temperature, pH, Ca^{2+} , and light)-triggered sol-gel transition of single-component supramolecular hydrogels. Detailed dynamic structural changes during the gel transition were visualized by preferential staining of the hydrophobic domains of hydrogel fibers. Fluctuation of short fibers in the sol state and fixation of long fibers in the gel state were observed by merging images recorded at different times. Real-time imaging showed a dynamic fusion of short fibers into long fibers during the sol-gel transition, leading to the formation of more crosslinking points (Fig. 8b). These conclusions demonstrated the holding and releasing ability of the designed supramolecular hydrogel, and therefore, four types of logic-gate functions (AND, OR, NAND, and NOR) were constructed by combining the different responsivenesses. Implementation of logic-gate functions into intelligent supramolecular hydrogels highlighted the



potential applications in multiresponsive drug delivery and release systems⁵⁰.

In situ fabrication of supramolecular hydrogel nanofibers at the oil/water interface was accomplished by self-assembly of a Schiff base hydrogelator synthesized from water-soluble and hydrophobic precursors. Emulsion droplets stabilized by hydrogel nanofibers showed a gel-sol transition in response to elevated temperature and increased acidity. By staining the hydrophobic domains of nanofibers and the oil phase with selected fluorophores, the stable structure of emulsion droplets coated by nanofibers could be imaged by CLSM. The dynamic fusion process of emulsion droplets triggered by external stimuli was visualized by real-time colocalization of droplets labeled by different colored fluorophores (Fig. 9a). Based on these observations, stimuli-triggered disassembly of the interfacial nanofibers was utilized to control a synthetic Cu-free click reaction confined in emulsion microreactors⁵¹. A new preparation method for producing homogeneous and reproducible supramolecular hydrogels was proposed based on the uniform pH change controlled by hydrolysis of glucono- δ -lactone (GdL). The slow GdL hydrolysis resulted in homogeneous hydrogel networks composed of fluorenylmethoxycarbonyl (Fmoc) dipeptides regardless of shear or mixing history, allowing the gelation mechanism to be monitored. In situ and real-time confocal imaging of the gelation process showed that Fmoc-dipeptides quickly started to aggregate into fibrillar structures, demonstrating that initial self-assembly was driven by π - π stacking (Fig. 9b). In comparison, inhomogeneous hydrogels with visibly suspended regions were achieved by pH adjustment using

HCl because the gelation kinetics were of the same order or faster than the mixing kinetics. This synthetic method offered the potential to prepare supramolecular hydrogels with uniform and consistent initial states for sample comparison in different systems⁵². Catalytic control over gelation time and stiffness of a low-molecular-weight hydrogel formed by a hydrazone-based hydrogelator was studied by a detailed protocol. After incorporation of fluorescein-derived fluorophores functionalized with aldehydes into the fiber formation process, the final morphology of the hydrogel network was visualized by CLSM. Fluorescence micrographs showed acidic catalysis at pH 5.0, and nucleophilic catalysis with aniline led to dense networks with thin highly branched fibers, while the uncatalyzed sample had a poorly connected network with apparently bundled fibers at pH 7 (Fig. 9c). These microscopic observations matched well with the macroscopic mechanical results measured by rheology⁵³. Functionalized supramolecular hydrogel networks encapsulating microemulsions were studied by fluorescence imaging to screen the real-time, dynamic changes in emulsion shapes. A novel drug delivery platform with a tunable postproduction release rate was constructed by self-assembly of a supramolecular hydrogel with three components. In this system, a hydrogel network was assembled by a fluorophore-conjugated hydrogelator to encapsulate thermoresponsive liposomes containing a proteolytic enzyme. Multicolor fluorescence imaging of the three components showed that neither hydrogel fibers nor trapped enzymes interfered with the giant multilamellar liposomes, indicating orthogonal self-assembly (Fig. 9d). A linear relationship between the concentration



of proteolytic enzyme and the hydrolysis degree of the fluorophore-conjugated hydrogelator was validated by fluorescence microscopy. Thus, the postproduction release rate of the system could be tuned by the heating time at constant temperature, facilitating applications for personalized drug release⁵⁴.

Self-sorting events of supramolecular hydrogels

To mimic living cells containing well-organized and stimuli-responsive systems with sophisticated functions, a multicomponent supramolecular hydrogel consisting of a peptide hydrogelator and an amphiphilic phosphate was designed and synthesized. Self-sorting events of supramolecular hydrogel nanofibers were comprehensively studied by in situ and real-time imaging with CLSM and STED. Selective labeling of a synthetic hydrogelator pair (peptide-type BPmocF₃ and lipid-type Phos-cycC₆) with appropriate fluorophores enabled the direct visualization of orthogonal self-assembly in the hydrogel network

(Fig. 10a). In situ time-lapse imaging demonstrated that the two hydrogelators behaved independently with different growth rates during the formation process. The high self-sorting degree quantitatively evaluated by Pearson's correlation coefficients indicated the negligible correlation between individual fibers, implying a highly orthogonal network. Stochastic nonsynchronous fiber formation visualized during the seed experiment indicated that the fiber growth rate was determined by the nucleation process, suggesting a cooperative mechanism. These findings demonstrated the significantly different driving forces of BPmocF₃ (π -interactions and hydrogen bonding) and Phos-cycC₆ (van der Waals interactions and hydrogen bonding) for self-sorting formation rather than coassembly⁵⁵. Using the same synthetic hydrogelator pair, fluorescence imaging of the orthogonal coassembly illustrated that the self-sorting phenomena were controlled by two crucial factors: (i) the surface charge of the hydrogelators and (ii) hydrophobicity of the

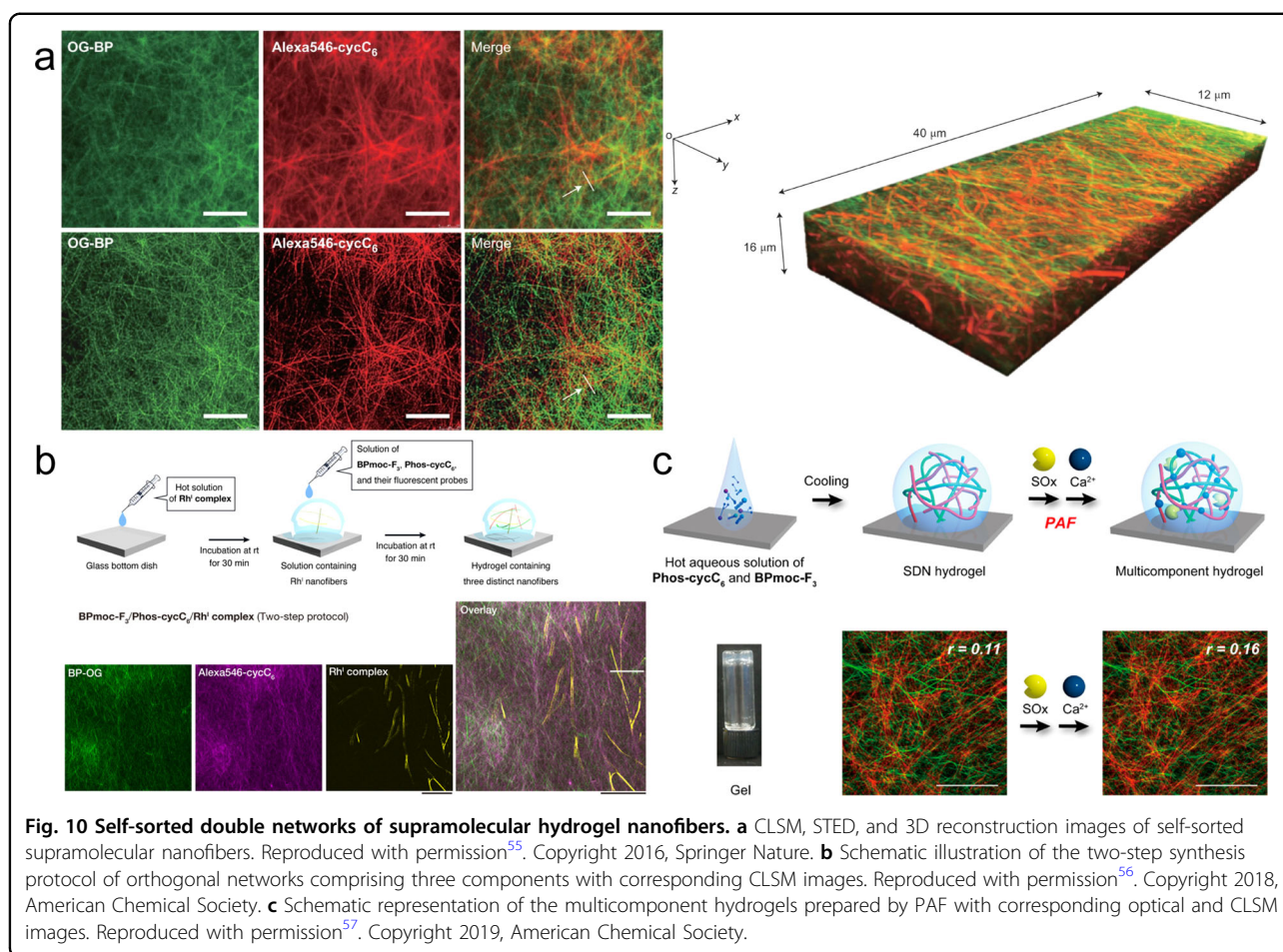


Fig. 10 Self-sorted double networks of supramolecular hydrogel nanofibers. **a** CLSM, STED, and 3D reconstruction images of self-sorted supramolecular nanofibers. Reproduced with permission⁵⁵. Copyright 2016, Springer Nature. **b** Schematic illustration of the two-step synthesis protocol of orthogonal networks comprising three components with corresponding CLSM images. Reproduced with permission⁵⁶. Copyright 2018, American Chemical Society. **c** Schematic representation of the multicomponent hydrogels prepared by PAF with corresponding optical and CLSM images. Reproduced with permission⁵⁷. Copyright 2019, American Chemical Society.

side chain on the peptide-type hydrogelators. The same net/surface charge of the hydrogelator pair and less hydrophobic side chains of peptide-type hydrogelators contributed to the formation of self-sorting nanofibers. Based on these findings, an orthogonal hydrogel network composed of three distinct sets of nanofibers (peptide-type hydrogelator, lipid-type hydrogelator, and cationic organorhodium complex) was first fabricated and visualized (Fig. 10b)⁵⁶. These observations of orthogonal hydrogel networks and self-sorting formation dynamics promoted the development of multicomponent soft materials with programmed functions for wider applications in intelligent biomimetics, optoelectronic devices, and biomedical treatment.

Based on the self-sorting double network (SDN) formed by Phos-cycC₆ and BPmocF₃, a multiresponsive system was designed for controlled protein release. Orthogonal SDN was fabricated by sequential addition of sarcosine oxidase (SOx) and Ca²⁺ ions into the gelator pair via a postassembly fabrication (PAF) protocol (Fig. 10c). In comparison, fluorescence imaging showed that only an inhomogeneous suspension containing precipitates was obtained by a one-step mixing protocol. Fluorescence

recovery after photobleaching (FRAP) analysis of time-course CLSM images indicated that the fluidity of Phos-cycC₆ nanofibers was suppressed by Ca²⁺ ions owing to coordination bonding. The addition of adenosine triphosphate could break the coordination bonds due to a stronger affinity and thus cause the gel-sol transition of the Phos-cycC₆/Ca²⁺ fibers. Moreover, the addition of sarcosine induced the gel-sol transition of BPmocF₃/SOx nanofibers by oxidation of BPmocF₃. An AND logic-gate fashion for antibody release was established based on the gel-sol transition of the multicomponent hydrogel in response to ATP and sarcosine⁵⁷. Another SDN supramolecular hydrogel was developed by the combination of peptide-type (NPmoc-F(4-F)F, derived from BPmocF₃) and lipid-type (Phos-cycC₆) hydrogelators, showing orthogonal responses to independent stimuli. High orthogonality of the SDN was confirmed by the above-mentioned Pearson's correlation coefficients of the CLSM images of hydrogelators stained by synthetic fluorophores. Investigation of the stimuli response demonstrated that the NPmoc moiety of NPmoc-F(4-F)F could be eliminated by appropriate reducing reagents to induce gel-sol transition. Moreover, hydrolysis of Phos-cycC₆ could be

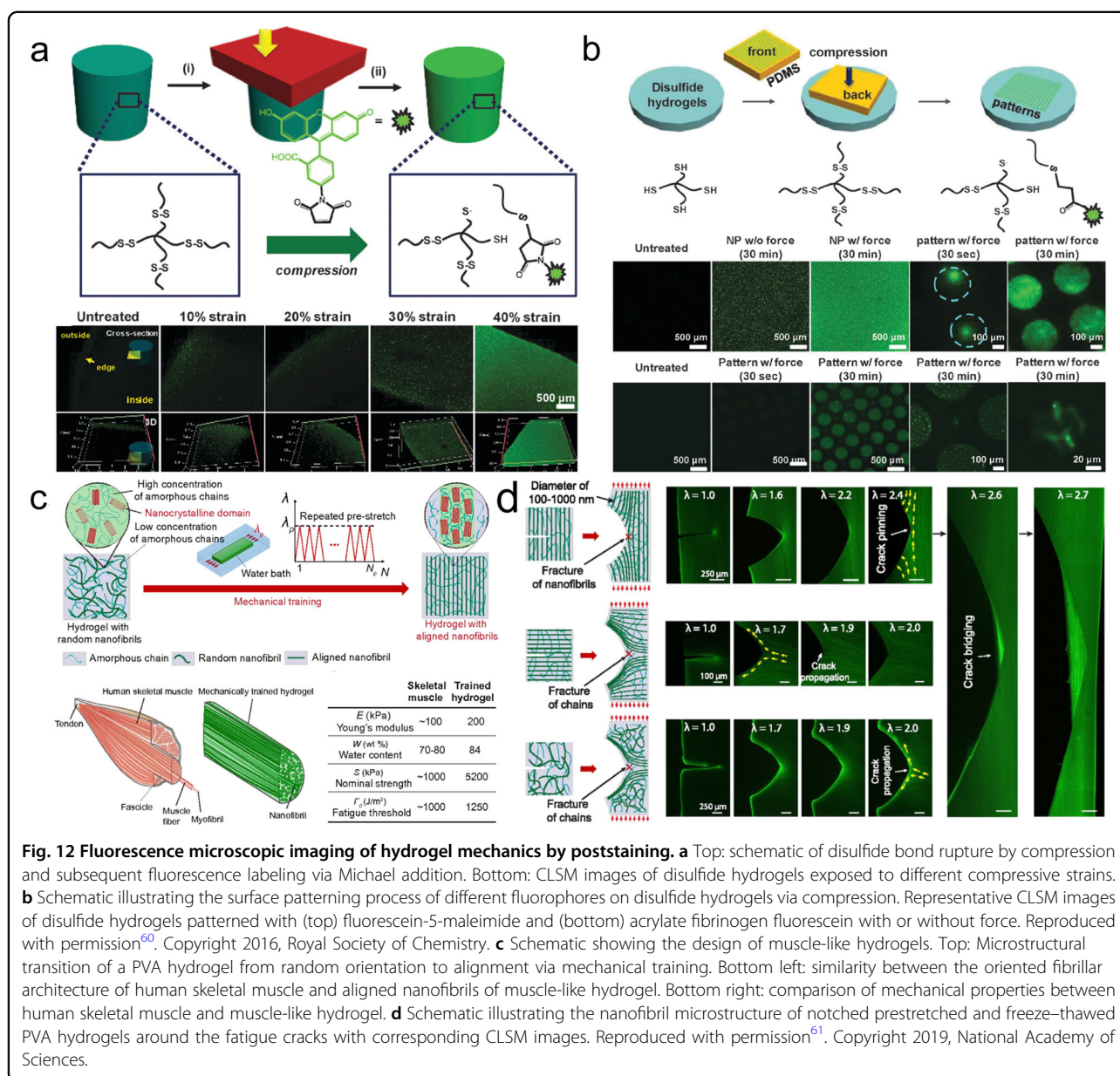


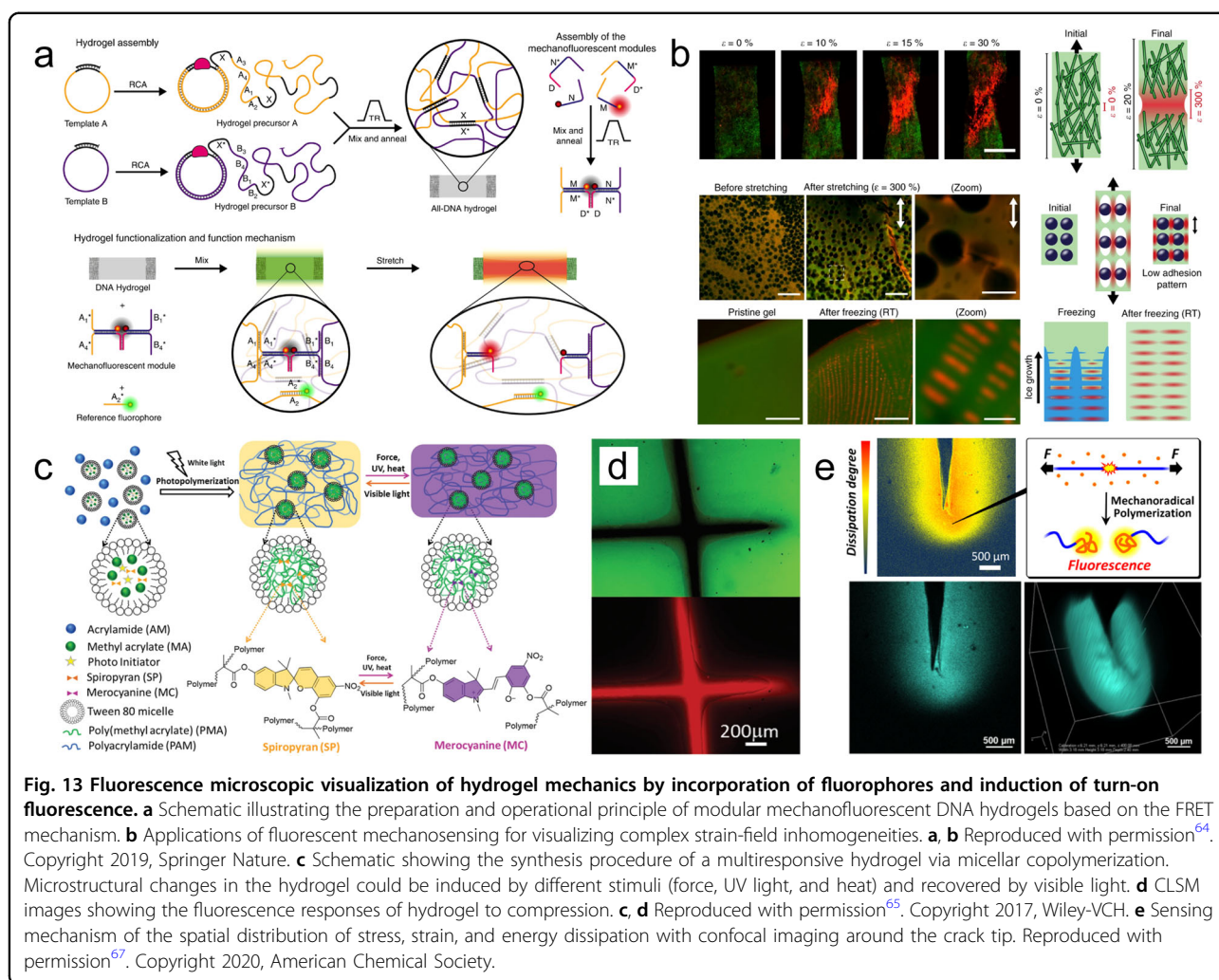
Fig. 12 Fluorescence microscopic imaging of hydrogel mechanics by poststaining. **a** Top: schematic of disulfide bond rupture by compression and subsequent fluorescence labeling via Michael addition. Bottom: CLSM images of disulfide hydrogels exposed to different compressive strains. **b** Schematic illustrating the surface patterning process of different fluorophores on disulfide hydrogels via compression. Representative CLSM images of disulfide hydrogels patterned with (top) fluorescein-5-maleimide and (bottom) acrylate fibrinogen fluorescein with or without force. Reproduced with permission⁶⁰. Copyright 2016, Royal Society of Chemistry. **c** Schematic showing the design of muscle-like hydrogels. Top: Microstructural transition of a PVA hydrogel from random orientation to alignment via mechanical training. Bottom left: similarity between the oriented fibrillar architecture of human skeletal muscle and aligned nanofibrils of muscle-like hydrogel. Bottom right: comparison of mechanical properties between human skeletal muscle and muscle-like hydrogel. **d** Schematic illustrating the nanofibril microstructure of notched prestretched and freeze-thawed PVA hydrogels around the fatigue cracks with corresponding CLSM images. Reproduced with permission⁶¹. Copyright 2019, National Academy of Sciences.

photolithography, specific fluorescent patterns on the hydrogel surface could be obtained by compression (Fig. 12b). One potential application of this technique was to decorate hydrogel surfaces with protein ligands for confinement of cells in patterned domains⁶⁰. For desirable applications in artificial tissues and soft devices, muscle-like PVA hydrogels were mechanically trained to obtain a high water content, high fatigue resistance, high strength, and superior compliance (Fig. 12c). The oriented alignment of nanofibrils obtained by mechanical training was directly visualized by confocal imaging of conjugated fluorophores by poststaining. Visualization of the fracturing process revealed that the fatigue resistance of the hydrogels originated from crack pinning by the

orientation of nanofibrils, which required much higher energy to fracture than amorphous polymer chains (Fig. 12d). These strong, soft, and fatigue-resistant hydrogels were applied to fabricate mechanically enhanced the microstructures through 3D printing followed by mechanical training⁶¹.

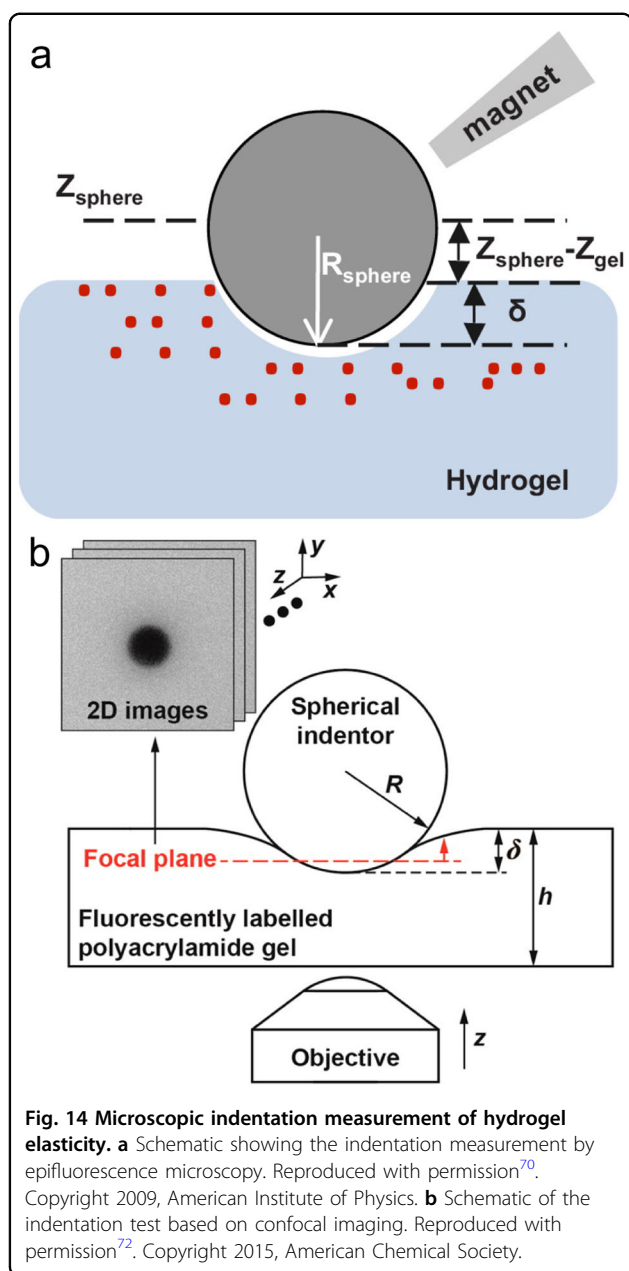
Incorporation of fluorophores

The poststaining method was incapable of in situ and real-time visualization, hence, strategies employing FRET pairs as indicators and mechanofluorophores as cross-linkers were proposed. Based on the thiol-Michael-type addition reaction, mechanoresponsive hydrogel particles were synthesized by droplet microfluidics. In this strategy,



a FRET pair composed of fluorophores modified with a maleimide moiety was fixed to the backbone of thiol-functionalized PEG. The external compression force induced a closer distance between the donor and acceptor, resulting in a fluorescence shift. On this basis, global network deformations were presented by CLSM images in true colors, and further localized deformations on the hydrogel particle surface were determined by combination with atomic force microscopy (AFM). This easy-to-read-out mechanosensitive matrix based on hydrogel particles was anticipated to probe transient forces and stress distribution in a dynamic cell environment⁶². Using the same FRET-sensing mechanism, a mechanochromic protein-hydrogel hybrid was designed for visualization of mechanical strain. In this synthetic hydrogel hybrid, fibronectin labeled with a FRET pair was terminally functionalized with an azide moiety and then conjugated to the PNIPAM network through a strain-promoted azide-alkyne cycloaddition reaction. Droplets containing hydrogel precursors were spotted onto unstretched

PDMS sheets and then polymerized for strain measurements. Pixel-by-pixel analysis of the CLSM images showed a significant decrease in the FRET ratio in hydrogel droplets during stretching of the PDMS sheet. These data validated that macroscopic deformation of the hydrogel droplet resulted in molecular conformation changes of the FRET pair interconnected to the hydrogel network. This synthetic hydrogel was envisioned to become a mechanosensor of biomolecules, cells, and tissues in bioengineering and mechanobiology⁶³. Programmable mechanofluorescent DNA hydrogels were fabricated by incorporation of FRET-based and tunable DNA tension probes into a 3D all-DNA hydrogel matrix. These mechanochromic DNA probes based on FRET pairs were synthesized by facile hybridization-driven functionalization. By breaking the sacrificial duplex of the DNA probes maintained in close proximity, fluorescence readouts were obtained to evaluate the reversible and irreversible strains (Fig. 13a). This modular hydrogel mechanosensor was applied to the microscopic 3D strain



mapping of subtle mechanical behaviors by CLSM (Fig. 13b). For example, microstructural failure mechanisms of hydrogel composites and stress distribution of ice-templated growth were visualized by 3D fluorescence imaging⁶⁴.

Induction of turn-on fluorescence

A multiresponsive fluorophore such as spiropyran (SP) changes its color and fluorescence by light, heat, and force stimuli through a reversible structural transformation from SP to merocyanine (MC), which can be recovered by irradiation with visible light. Taking advantage of SP, a micelle-assisted copolymerization method was reported

to fabricate thermoresponsive, photoresponsive, and mechanoresponsive hydrogels (Fig. 13c). External stimuli-induced color and fluorescence changes of SP allowed a visible indication of local network deformation. In particular, the high fluorescence contrast generated from the SP-MC transition could be further applied to investigate microscale deformation by in situ confocal imaging (Fig. 13d). These unique optical properties of multistimuli-responsive hydrogels showed great potential for sensing, imaging, and display applications⁶⁵. Another recent work reported the usage of Diels-Alder adducts of π -extended anthracenes as mechanofluorophore crosslinkers of PNIPAM hydrogel networks. Scission of covalent bonds was directly imaged with CLSM and quantified by fluorescence intensity correlating to macroscopic fracture mechanics and the elasticity tested by uniaxial compression. It was elucidated that the dissolution of hydrogen bonds in the hydrogel network at a high water content weakened the stress distribution, leading to reduced mechanical performance and higher crack incidence⁶⁶. Although covalent bond scission was visualized and quantified by incorporation of mechanophores into the hydrogel networks, there were several limitations (e.g., incorporation-induced structural changes, hydrophobicity of mechanophores, formation of weaker scissile bonding, and high cost of synthesis) of this technique to be overcome. Thus, a mechanoradical polymerization technique was designed to visualize and quantify polymer strand scission in the damage zone of double-network hydrogels (Fig. 13e). The second network in this strategy was formed by polymerization of NIPAM initiated by mechanoradicals generated from covalent bond scission. Upon heating above the lowest critical solution temperature (LCST) of PNIPAM, fluorophores trapped in the hydrophobic domains of PNIPAM could visualize the spatial distribution of stress, strain, and energy dissipation around the crack tip. Quantitative estimation of the mechanical energy density in the damage zone was achieved by fluorescence intensity mapping or line profile analysis calibrated with tensile testing⁶⁷.

Elasticity measurement by fluorescence imaging

During the past two decades, researchers have performed a large number of studies on the interfacial adhesion between cells and extracellular matrices (ECMs). Although the elastic substrate method can quantitatively report the direction, location, and magnitude of these interfacial stresses, measurement of mammalian cell movement is difficult because of the mismatch between the mechanical properties of elastomers and mobility rates of mammalian cells. Therefore, PAM substrates were adopted as substitutions since their stiffness could be readily regulated by different concentrations of monomers and crosslinkers. However, it is inappropriate

Table 2 List of the microscopic visualization strategies of functionalized hydrogels.

Hydrogel	Fluorescent marker	Research subject	Refs.
PVA	DTAF	Porous and 3D networks	16–18
PNIPAM/PVP	Cy5/Cy3	Multiple-scale morphology of interpenetrated networks	20
PVA	Rh110, RBITC, FITC	Semi-interpenetrated networks and matter exchange	21,22
Fibrin	Alexa Fluor 595	Fibril diameter, porosity, and alignment	23
Fibrin	Alexa Fluor 488	Structural, diffusional, and mechanical characteristics of fibrin	24
Collagen	TRITC	Structural and mechanical properties of the 3D scaffolds	25
Agarose	DTAF	Homogeneity of the interpenetrated networks	26
Low acyl gellan	DTAF	Microstructures in mixed hydrogel systems	27
XG/GB	DTAF/Nile Blue A	Influences of pH and ionic strength on networks	28
Polysaccharides	DTAF/Rhodamine B	Component distribution and compatibility of mixed hydrogel systems, network formation	29
DMA	DAPI/Perylene Red	Shape memory effect of organohydrogel networks	30–33
GalNAc-aa derivatives	HANBD, ANS, rhodamine, synthetic fluorophores	Fibrous networks, thermoresponsive release and capture, fluorometric hydrogel array, pH-triggered controlled release, molecular recognition systems	34–39
β^3 -tripeptide	Synthetic fluorophores	Self-assembling helical structure and in vivo animal imaging	40
I ₃ K peptide	Alexa Fluor 647, Cy3B	Self-assembly processes of helical fibrils	41
Phospholipids, oleic acid	DPPE-Rhodamine B	Spongy morphology of hydrogel networks	42
CS	Autoluminescence, FITC, TPE	Mechanisms of gelation process and hierarchically oriented structure	43–46
Laponite/FMMT	Rhodamine 6 G, rhodamine B	Kinetics of gelation process and inorganic hydrogel composites	47
Collagen	ATTO 647 N	Fibrillogenesis during sol-gel transition	48
BPmocF ₃ Phos-cycC ₆ NPmoc-F(4-F)F	C ₁₈ -rhodamine, fluorescent beads, OG-BP, Alexa546-cycC ₆ , NBD-cycC ₆ , NP-Alexa647	Sol-gel transition in response to stimuli, Brownian motion of matter in the networks, formation dynamics of orthogonal self-assembly, self-sorting events, controlled protein release	49,50,55–58
Synthetic gelators	ANS, Nile-red, NBD-C12	Stimuli-induced fusion of microdroplets in the networks	51
Fmoc-dipeptides	Nile Blue Sulfate	Controlled gelation process of the gelators	52
Low-molecular-weight gelators	Fluorescein derivative	Catalytic control over self-assembly of the gelators	53
Low-molecular-weight gelators	Fluorescein, NBD, rhodamine	Orthogonal self-assembly of the gelators, postproduction release	54
Low-molecular-weight gelators	Synthetic fluorophores	Compartmentalization of multicomponents in the networks	59
PEG	Fluorescein	Force-driven bond rupture in the networks	60
PVA	DTAF	Oriented alignment and fracturing process of nanofibrils	61
PEG	Alexa Fluor 488, Alexa Fluor 555	Global and localized network deformation	62
PNIPAM/PEG/ Fibronectin	Alexa Fluor 488, Alexa Fluor 546	Macroscopic deformation induced molecular conformation changes in the networks	63
DNA hydrogels	Atto488, Atto565	Reversible and irreversible strains, 3D strain mapping	64
Poly(AM-co-MA)	Spiropyran	Localized network deformation	65
PNIPAM	Synthetic mechanophore	Scission of covalent bonds in the networks	66

Table 2 continued

Hydrogel	Fluorescent marker	Research subject	Refs.
PNaAMPS/PAM/ PNIPAM	ANS	Polymer strand scission in the damage zone of the networks	67
PAM	Fluorescent beads	Hydrogel elasticity	68–72

PVA poly(vinyl alcohol), DTAF 5-(4,6-dichlorotriazinyl) aminofluorescein, PNIPAM poly(*N*-isopropylacrylamide), PVP poly(vinyl pyrrolidone), Rh110 Rhodamine 110, RBITC Rhodamine B isothiocyanate, FITC fluorescein isothiocyanate, TRITC tetramethylrhodamine-5-(and-6)-isothiocyanate, XG xanthan gum, GB gelatin B, DMA *N,N*-dimethylacrylamide, DAPI 6-Diamidino-2-phenylindole dihydrochloride, Perylene Red *N,N*-Bis (2,6-diisopropylphenyl)-1,6,7,12-tetraphenoxy-3,4,9,10-perylene-tetracarboxylic diimide, GalNAC-aa *N*-acetyl-galactosamine-appended amino acid, HANBD nitrobenzoxadiazole derivative, ANS 8-anilino-1-naphthalenesulfonic acid, CS chitosan, TPE tetraphenylethene, FMMT fractionated montmorillonite, NBD nitrobenzoxadiazole, Fmoc-dipeptides fluorenylmethoxycarbonyl dipeptides, C₁₈-rhodamine octadecylrhodamine B chloride, PEG poly(ethylene glycol), poly(AM-co-MA/SP) polyacrylamide-co-methyl acrylate, PNaAMPS poly(2-acrylamido-2-methylpropane sulfonic acid sodium salt), PAM polyacrylamide, BPmocF₃, Phos-cycC₆, NPmoc-F(4-F)F, OG-BP, Alexa546-cycC₆, NBD-cycC₆, NP-Alexa647, and NBD-C12 are synthetic compounds.

to measure the elasticity of PAM substrates by macroscopic stretch tests because of their microscale thickness. Therefore, earlier microscopic measurements based on fluorescence imaging emerged. Fluorescent latex marker beads were embedded throughout the PAM substrate to determine the *z*-position of the hydrogel surface. The PAM substrate was sandwiched between glass surfaces and then compressed by small metal weights. The obtained change in thickness along with the known compressing force was used to calculate the elasticity of the PAM substrate⁶⁸. Another measuring strategy of hydrogel ECM elasticity was proposed based on indentation of the substrates and fluorescence imaging of the resulting deformation. In this strategy, a steel sphere of known density and radius was deposited onto the hydrogel substrate to generate surface deformation and then removed by a magnet. The indentation depth was determined by the change in vertical position of fluorescent markers embedded in the hydrogel matrix. The hydrogel elasticity calculated by the Hertzian pressure method was more accurate for compliant gels but less accurate for stiff gels⁶⁹. To avoid possible damage during removal of the indenter, an improved method was reported by determining the *z*-positions of the diameter of the sphere (Fig. 14a). More importantly, a wider range of accuracy of this method was acquired by matching the elasticity of the hydrogel substrate with the density of the appropriate indenter. The calculated elasticity values were in order-of-magnitude agreement with AFM measurements, indicating the potential for quality control during fabrication of many hydrogel ECMs⁷⁰.

Although the Hertz contact model was adopted throughout the development of microscopic indentation methods, the limitations of this model were usually overlooked to overestimate the elasticity of substrates. In Hertz contact theory, the substrate is assumed to be a linear elastic half-space with an infinite depth, whereas in fact, the thickness of the substrate is comparable to the contact radius or indenter radius. Therefore, the non-linearity of the hydrogel substrate and large deformation were taken into consideration, and the Hertz contact

model was modified by a correction factor using a finite-element method⁷¹. Another major deviation of the above methods originated from indentation depth measurement because the fluorescent beads on the contact plane need to be identified with human eyes. Recent work reported a solution to this problem using CLSM since the *z*-position of each image slice was recorded during 3D imaging. 3D reconstruction images provided information on the indented profile and contact radius for selection of the appropriate contact mechanics models (Fig. 14b). Benefiting from the development of an automatic measuring procedure, the measurement of indentation depth could be user-independent to eliminate individual error. Additionally, high-throughput multipoint indentation could be facilitated if a detecting array was established⁷².

Conclusions and future perspectives

The past few decades have witnessed the phenomenal advancements of fluorescence microscopy and its broad applications in material science. In this review, we provide a brief summary of the recent advances in the visualization of functionalized hydrogels by fluorescence microscopy (Table 2). These intriguing examples are anticipated to shed light on the concepts, mechanisms, and applications of fluorescence visualization strategies for functionalized hydrogels. To tackle the potential challenges of this subject, current limitations, possible solutions, and future perspectives should be taken into careful consideration.

As summarized in the above discussion, researchers focused most attention on the visualization of intrinsic hydrogel systems but neglected the importance of hydrogel composite systems. Structural visualization and applications of organic–organic hydrogel composites consisting of interpenetrated or semi-interpenetrated networks have already been discussed in detail^{17,18,20–22}. Future research should be focused on organic–inorganic hydrogel composites because of their enhanced optical and mechanical properties, among others. In recent years, the modification of inorganic fillers, such as graphene, nanoclays, and layered double hydroxides with

fluorophores, has been widely reported. Hence, the spatial distribution, anisotropic arrangement, and interfacial interaction of inorganic fillers within hydrogel composites are expected to be visualized to improve their chemical, physical, and biological performance.

Quantification of matter transport is an important issue in practical applications (e.g., drug release, pollutant removal, and substance separation) of functionalized hydrogels. However, only a few groups have tried to visualize the Brownian motion of fluorescent nanobeads^{49,58} within hydrogel networks or utilize FRAP^{22,57} to analyze the fluidity of hydrogel nanofibers. The reason is that researchers have paid attention to qualitative visualization rather than further quantification analysis. In fact, there are a variety of quantification methods based on fluorescence microscopic imaging⁷³, such as FRAP, inverse FRAP, fluorescence loss in photobleaching, fluorescence localization after photobleaching, and fluorescence correlation spectroscopy⁷⁴. Rational utilization of these methods under appropriate circumstances could deepen the comprehension of the visualized transport process to promote the efficiency and performance of functionalized hydrogels.

It is worth noting that the most prevailing microscopic technique for visualizing functionalized hydrogels is currently CLSM. Thus, wider applications of super-resolution techniques remain to be exploited and developed for the observation of hydrogel microstructures at higher resolution. The high cost of complex instruments and lack of appropriate fluorescent markers are considered major obstacles. The rapid development and growing popularization of various super-resolution microscopies, such as STED⁹, STORM¹⁰, photoactivated localization microscopy⁷⁵, and structured illumination microscopy⁷⁶, represent possible solutions to the former problem. The latter problem could be solved by the design and synthesis of ultrastable fluorophores, such as quantum dots, metal nanoclusters, and carbonaceous nanoparticles.

Among all the abovementioned examples, only a few studies have reported the coupling of CLSM with CRM, AFM, and confocal rheology. Therefore, coupling techniques based on fluorescence microscopy and other characterization methods need further development. The greatest challenge is the integration of confocal imaging systems with other detection, measurement, and visualization systems. To overcome this difficulty, developers from different disciplines, such as optics, mechanics, and electronics, must work together to design and build advanced instruments. One successful example is correlative light and electron microscopy⁷⁷ combining fluorescence microscopy and electron microscopy, which is capable of providing positional information and visualizing refined microstructures simultaneously.

Overall, this review may offer viable opportunities and inspiration for material researchers to design new strategies for studying functionalized hydrogels. Additionally, we predict that the unprecedented progress of fluorescence microscopy techniques will contribute to a fundamental revolution for characterizing not only functionalized hydrogels but also various polymeric materials in the near future.

Acknowledgements

This research was supported by the National Key R&D Program of China (2017YFA0207800), the National Natural Science Funds for Distinguished Young Scholar (21725401), the National Natural Science Foundation (22161142021), the 111 projects (B14009), and the Fundamental Research Funds for the Central Universities.

Author contributions

All the authors contributed to the writing, review, and editing of the manuscript.

Competing interests

The authors declare no competing interests.

Publisher's note

Springer Nature remains neutral with regard to jurisdictional claims in published maps and institutional affiliations.

Received: 10 October 2021 Revised: 12 January 2022 Accepted: 17 January 2022.

Published online: 6 May 2022

References

- Zhao, Z., Fang, R., Rong, Q. & Liu, M. Bioinspired nanocomposite hydrogels with highly ordered structures. *Adv. Mater.* **29**, 1703045 (2017).
- Wang, H. & Heilshorn, S. C. Adaptable hydrogel networks with reversible linkages for tissue engineering. *Adv. Mater.* **27**, 3717–3736 (2015).
- Vashist, A., Vashist, A., Gupta, Y. K. & Ahmad, S. Recent advances in hydrogel based drug delivery systems for the human body. *J. Mater. Chem. B* **2**, 147–166 (2014).
- Oran, D. et al. 3D nanofabrication by volumetric deposition and controlled shrinkage of patterned scaffolds. *Science* **362**, 1281–1285 (2018).
- Zhao, Y. et al. Soft phototactic swimmer based on self-sustained hydrogel oscillator. *Sci. Robot.* **4**, eaax7112 (2019).
- Yu, G., Yan, X., Han, C. & Huang, F. Characterization of supramolecular gels. *Chem. Soc. Rev.* **42**, 6697–6722 (2013).
- Lichtman, J. W. & Conchello, J.-A. Fluorescence microscopy. *Nat. Methods* **2**, 910–919 (2005).
- Conchello, J.-A. & Lichtman, J. W. Optical sectioning microscopy. *Nat. Methods* **2**, 920–931 (2005).
- Vicidomini, G., Bianchini, P. & Diaspro, A. STED super-resolved microscopy. *Nat. Methods* **15**, 173–182 (2018).
- Dempsey, G. T., Vaughan, J. C., Chen, K. H., Bates, M. & Zhuang, X. Evaluation of fluorophores for optimal performance in localization-based super-resolution imaging. *Nat. Methods* **8**, 1027–1036 (2011).
- Klar, T. A., Jakobs, S., Dyba, M., Egner, A. & Hell, S. W. Fluorescence microscopy with diffraction resolution barrier broken by stimulated emission. *Proc. Natl Acad. Sci. USA* **97**, 8206–8210 (2000).
- Betzig, E. et al. Imaging intracellular fluorescent proteins at nanometer resolution. *Science* **313**, 1642–1645 (2006).
- Yao, J., Yang, M. & Duan, Y. Chemistry, biology, and medicine of fluorescent nanomaterials and related systems: new insights into biosensing, bioimaging, genomics, diagnostics, and therapy. *Chem. Rev.* **114**, 6130–6178 (2014).
- Shaner, N. C., Steinbach, P. A. & Tsien, R. Y. A guide to choosing fluorescent proteins. *Nat. Methods* **2**, 905–909 (2005).

15. Biju, V., Itoh, T. & Ishikawa, M. Delivering quantum dots to cells: bioconjugated quantum dots for targeted and nonspecific extracellular and intracellular imaging. *Chem. Soc. Rev.* **39**, 3031–3056 (2010).
16. Fergg, F., Keil, F. J. & Quader, H. Investigations of the microscopic structure of poly(vinyl alcohol) hydrogels by confocal laser scanning microscopy. *Colloid Polym. Sci.* **279**, 61–67 (2001).
17. Bodugoz-Senturk, H. et al. The effect of polyethylene glycol on the stability of pores in poly(vinyl alcohol) hydrogels during annealing. *Biomaterials* **29**, 141–149 (2008).
18. Bodugoz-Senturk, H., Macias, C. E., Kung, J. H. & Muratoglu, O. K. Poly(vinyl alcohol)–acrylamide hydrogels as load-bearing cartilage substitute. *Biomaterials* **30**, 589–596 (2009).
19. Rust, M. J., Bates, M. & Zhuang, X. Sub-diffraction-limit imaging by stochastic optical reconstruction microscopy (STORM). *Nat. Methods* **3**, 793–795 (2006).
20. Gilbert, T. et al. Nanostructure of fully injectable hydrazone–thiosuccinimide interpenetrating polymer network hydrogels assessed by small-angle neutron scattering and dSTORM single-molecule fluorescence microscopy. *ACS Appl. Mater. Interfaces* **9**, 42179–42191 (2017).
21. Bonelli, N., Montis, C., Mirabile, A., Berti, D. & Baglioni, P. Restoration of paper artworks with microemulsions confined in hydrogels for safe and efficient removal of adhesive tapes. *Proc. Natl Acad. Sci. USA* **115**, 5932–5937 (2018).
22. Mastrangelo, R. et al. Twin-chain polymer hydrogels based on poly(vinyl alcohol) as new advanced tool for the cleaning of modern and contemporary art. *Proc. Natl Acad. Sci. USA* **117**, 7011–7020 (2020).
23. Dubey, N., Letourneau, P. C. & Tranquillo, R. T. Neuronal contact guidance in magnetically aligned fibrin gels: effect of variation in gel mechano-structural properties. *Biomaterials* **22**, 1065–1075 (2001).
24. Leonidakis, K. A. et al. Fibrin structural and diffusional analysis suggests that fibers are permeable to solute transport. *Acta Biomater.* **47**, 25–39 (2017).
25. Cross, V. L. et al. Dense type I collagen matrices that support cellular remodeling and microfabrication for studies of tumor angiogenesis and vasculogenesis in vitro. *Biomaterials* **31**, 8596–8607 (2010).
26. Russ, N., Zielbauer, B. I., Koynov, F. & Vilgis, T. A. Influence of nongelling hydrocolloids on the gelation of agarose. *Biomacromolecules* **14**, 4116–4124 (2013).
27. Norton, A. B., Hancocks, R. D., Spyropoulos, F. & Grover, L. M. Development of 5-(4,6-dichlorotriazinyl) amino fluorescein (DTAF) staining for the characterisation of low acyl gellan microstructures. *Food Hydrocoll.* **53**, 93–97 (2016).
28. Wang, C.-S., Natale, G., Virgilio, N. & Heuzey, M.-C. Synergistic gelation of gelatin B with xanthan gum. *Food Hydrocoll.* **60**, 374–383 (2016).
29. Khin, M. N., Ahammed, S. & Zhong, F. Development of 5-(4,6-dichlorotriazinyl) amino fluorescein (DTAF)-labelled polysaccharides for characterization of microstructure and phase distribution of composite hydrogel visualization of hydrogels using CLSM. *Food Biosci.* **41**, 100909 (2021).
30. Zhao, Z., Zhang, K., Liu, Y., Zhou, J. & Liu, M. Highly stretchable, shape memory organohydrogels using phase-transition microinclusions. *Adv. Mater.* **29**, 1701695 (2017).
31. Zhao, Z. et al. Biphasic synergistic gel materials with switchable mechanics and self-healing capacity. *Angew. Chem. Int. Ed.* **56**, 13464–13469 (2017).
32. Zhao, Z. et al. Dual-programmable shape-morphing and self-healing organohydrogels through orthogonal supramolecular heteronetworks. *Adv. Mater.* **30**, 1804435 (2018).
33. Zhao, Z. et al. Adaptive superamphiphilic organohydrogels with reconfigurable surface topography for programming unidirectional liquid transport. *Adv. Funct. Mater.* **29**, 1807858 (2019).
34. Kiyonaka, S., Sugiyasu, K., Shinkai, S. & Hamachi, I. First thermally responsive supramolecular polymer based on glycosylated amino acid. *J. Am. Chem. Soc.* **124**, 10954–10955 (2002).
35. Kiyonaka, S. et al. Semi-wet peptide/protein array using supramolecular hydrogel. *Nat. Mater.* **3**, 58–64 (2004).
36. Tamaru, S., Kiyonaka, S. & Hamachi, I. Three distinct read-out modes for enzyme activity can operate in a semi-wet supramolecular hydrogel. *Chem. Eur. J.* **11**, 7294–7304 (2005).
37. Zhou, S.-L. et al. pH-responsive shrinkage/swelling of a supramolecular hydrogel composed of two small amphiphilic molecules. *Chem. Eur. J.* **11**, 1130–1136 (2005).
38. Yamaguchi, S., Yoshimura, I., Kohira, T., Tamaru, S. & Hamachi, I. Cooperation between artificial receptors and supramolecular hydrogels for sensing and discriminating phosphate derivatives. *J. Am. Chem. Soc.* **127**, 11835–11841 (2005).
39. Wada, A., Tamaru, S., Ikeda, M. & Hamachi, I. MCM–enzyme–supramolecular hydrogel hybrid as a fluorescence sensing material for polyanions of biological significance. *J. Am. Chem. Soc.* **131**, 5321–5330 (2009).
40. Kulkarni, K. et al. β^3 -Tripeptides coassemble into fluorescent hydrogels for serial monitoring in vivo. *ACS Biomater. Sci. Eng.* **4**, 3843–3847 (2018).
41. Cox, H., Georgiades, P., Xu, H., Waigh, T. A. & Lu, J. R. Self-assembly of mesoscopic peptide surfactant fibrils investigated by STORM super-resolution fluorescence microscopy. *Biomacromolecules* **18**, 3481–3491 (2017).
42. Talló, K., Bosch, M., Pons, R., Cocera, M. & López, O. Preparation and characterization of a supramolecular hydrogel made of phospholipids and oleic acid with a high water content. *J. Mater. Chem. B* **8**, 161–167 (2020).
43. Nie, J. et al. Orientation in multi-layer chitosan hydrogel: morphology, mechanism, and design principle. *Sci. Rep.* **5**, 7635 (2015).
44. Sereni, N. et al. Dynamic structuration of physical chitosan hydrogels. *Langmuir* **33**, 12697–12707 (2017).
45. Wang, Z., Nie, J., Qin, W., Hu, Q. & Tang, B. Z. Gelation process visualized by aggregation-induced emission fluorogens. *Nat. Commun.* **7**, 12033 (2016).
46. Nie, J., Wang, Z. & Hu, Q. Difference between chitosan hydrogels via alkaline and acidic solvent systems. *Sci. Rep.* **6**, 1–8 (2016).
47. Pujala, R. K., Schneijdenberg, C. T. W. M., van Blaaderen, A. & Bohidar, H. B. In-situ observation of hierarchical self-assembly driven by bicontinuous gelation in mixed nanodisc dispersions. *Sci. Rep.* **8**, 5589 (2018).
48. Tran-Ba, K.-H., Lee, D. J., Zhu, J., Paeng, K. & Kaufman, L. J. Confocal rheology probes the structure and mechanics of collagen through the sol-gel transition. *Biophys. J.* **113**, 1882–1892 (2017).
49. Matsumoto, S. et al. Photo gel–sol/sol–gel transition and its patterning of a supramolecular hydrogel as stimuli-responsive biomaterials. *Chem. Eur. J.* **14**, 3977–3986 (2008).
50. Komatsu, H. et al. Supramolecular hydrogel exhibiting four basic logic gate functions to fine-tune substance release. *J. Am. Chem. Soc.* **131**, 5580–5585 (2009).
51. Nishida, Y. et al. In situ synthesis of a supramolecular hydrogelator at an oil/water interface for stabilization and stimuli-induced fusion of microdroplets. *Angew. Chem. Int. Ed.* **56**, 9410–9414 (2017).
52. Adams, D. J. et al. A new method for maintaining homogeneity during liquid–hydrogel transitions using low molecular weight hydrogelators. *Soft Matter* **5**, 1856–1862 (2009).
53. Poolman, J. M. et al. Variable gelation time and stiffness of low-molecular-weight hydrogels through catalytic control over self-assembly. *Nat. Protoc.* **9**, 977–988 (2014).
54. Boekhoven, J., Koot, M., Wezendonk, T. A., Eelkema, R. & van Esch, J. H. A self-assembled delivery platform with post-production tunable release rate. *J. Am. Chem. Soc.* **134**, 12908–12911 (2012).
55. Onogi, S. et al. In situ real-time imaging of self-sorted supramolecular nanofibers. *Nat. Chem.* **8**, 743–752 (2016).
56. Kubota, R. et al. Imaging-based study on control factors over self-sorting of supramolecular nanofibers formed from peptide- and lipid-type hydrogelators. *Bioconjugate Chem.* **29**, 2058–2067 (2018).
57. Tanaka, W. et al. Post-assembly fabrication of a functional multicomponent supramolecular hydrogel based on a self-sorting double network. *J. Am. Chem. Soc.* **141**, 4997–5004 (2019).
58. Shigemitsu, H. et al. An adaptive supramolecular hydrogel comprising self-sorting double nanofiber networks. *Nat. Nanotechnol.* **13**, 165–172 (2018).
59. Boekhoven, J. et al. Bio-inspired supramolecular materials by orthogonal self-assembly of hydrogelators and phospholipids. *Chem. Sci.* **7**, 6021–6031 (2016).
60. Lee, J., Silberstein, M. N., Abdeen, A. A., Kim, S. Y. & Kilian, K. A. Mechanochemical functionalization of disulfide linked hydrogels. *Mater. Horiz.* **3**, 447–451 (2016).
61. Lin, S., Liu, J., Liu, X. & Zhao, X. Muscle-like fatigue-resistant hydrogels by mechanical training. *Proc. Natl Acad. Sci. USA* **116**, 10244–10249 (2019).
62. Neubauer, J. W. et al. Mechanoresponsive hydrogel particles as a platform for three-dimensional force sensing. *ACS Appl. Mater. Interfaces* **11**, 26307–26313 (2019).
63. Taki, M., Yamashita, T., Yatabe, K. & Vogel, V. Mechano-chromic protein–polymer hybrid hydrogel to visualize mechanical strain. *Soft Matter* **15**, 9388–9393 (2019).
64. Merindol, R., Delechiave, G., Heinen, L., Catalani, L. H. & Walther, A. Modular design of programmable mechanofluorescent DNA hydrogels. *Nat. Commun.* **10**, 528 (2019).

65. Chen, H., Yang, F., Chen, Q. & Zheng, J. A novel design of multi-mechanoresponsive and mechanically strong hydrogels. *Adv. Mater.* **29**, 1606900 (2017).
66. Stratigaki, M. et al. Fractography of poly(*N*-isopropylacrylamide) hydrogel networks crosslinked with mechanofluorophores using confocal laser scanning microscopy. *Polym. Chem.* **11**, 358–366 (2020).
67. Matsuda, T., Kawakami, R., Nakajima, T. & Gong, J. P. Crack tip field of a double-network gel: visualization of covalent bond scission through mechanoradical polymerization. *Macromolecules* **53**, 8787–8795 (2020).
68. Dembo, M. & Wang, Y.-L. Stresses at the cell-to-substrate interface during locomotion of fibroblasts. *Biophys. J.* **76**, 2307–2316 (1999).
69. Damjanović, V., Lagerholm, B. C. & Jacobson, K. Bulk and micropatterned conjugation of extracellular matrix proteins to characterized polyacrylamide substrates for cell mechanotransduction assays. *Biotechniques* **39**, 847–851 (2005).
70. D'Sa, D. J. et al. High-throughput indentational elasticity measurements of hydrogel extracellular matrix substrates. *Appl. Phys. Lett.* **95**, 063701 (2009).
71. Long, R., Hall, M. S., Wu, M. & Hui, C.-Y. Effects of gel thickness on microscopic indentation measurements of gel modulus. *Biophys. J.* **101**, 643–650 (2011).
72. Lee, D., Rahman, M. M., Zhou, Y. & Ryu, S. Three-dimensional confocal microscopy indentation method for hydrogel elasticity measurement. *Langmuir* **31**, 9684–9693 (2015).
73. Ishikawa-Ankerhold, H. C., Ankerhold, R. & Drummen, G. P. C. Advanced fluorescence microscopy techniques—FRAP, FLIP, FLAP, FRET and FLIM. *Molecules* **17**, 4047–4132 (2012).
74. Hess, S. T., Huang, S., Heikal, A. A. & Webb, W. W. Biological and chemical applications of fluorescence correlation spectroscopy: a review. *Biochemistry* **41**, 697–705 (2002).
75. Manley, S. et al. High-density mapping of single-molecule trajectories with photoactivated localization microscopy. *Nat. Methods* **5**, 155–157 (2008).
76. Gustafsson, M. G. L. Surpassing the lateral resolution limit by a factor of two using structured illumination microscopy. *J. Microsc.* **198**, 82–87 (2000).
77. Perkovic, M. et al. Correlative light- and electron microscopy with chemical tags. *J. Struct. Biol.* **186**, 205–213 (2014).